FRICTION STIR PROCESSING OF 2xxx SERIES ALUMINIUM PM ALLOYS

By

James Adye

Submitted in partial fulfilment of the requirements
for the degree of Master of Applied Science

at

Dalhousie University
Halifax, Nova Scotia
April 2020

Table of Contents

List of Tables

List of Figures

Abstract

Friction stir welding (FSW) is a novel solid-state process known to facilitate the joining of materials that exhibit a poor response to conventional fusion welding technologies. Certain aluminium alloys in the 2xxx series are prime examples as their use in welded structures is desirable, but typically avoided in light of their acute sensitivity to solidification cracking. The desire to use these high strength alloys has historically resulted in less ideal joining methods such as brazing or riveting being implemented. To date, the majority of FSW research on these alloys has involved wrought products, leaving a clear void in the understanding of how those produced through aluminum powder metallurgy (APM) alloys respond. To address this shortfall, the response of two commercially relevant APM alloys denoted as PM2618 (Al-2.3Cu-1.6Mg-1Fe-1Ni-0.5Sn) and TC2000 (Al-1Mg-1.5Sn) to FSW was investigated in this study. The rotation speed and traverse rate of the tool were the principal process variables considered. In the PM2618 a variety of processing parameter combinations were found to produce defect-free welds when inspected through X-ray techniques coupled with metallographic inspection of polished cross sections. The stirred material was found to have a highly refined microstructure, showing an increase in hardness but without any apparent change to the nominal phase composition. Bend testing revealed significant improvements as a result of FSW. These included a near doubling of ductility, an average increase in yield strength in bending of 33%, and a 35% improvement in UBS. Bending fatigue behaviour was also investigated, with averaged gains of 27% measured relative to the as-sintered base material. Conversely, it was found that the TC2000 responded negatively to all processing parameter combinations used. While the stirred material in the microstructure exhibited a similar degree of refinement as seen in the PM2618, through X-ray examination it was found that specimen also contained tunnel defects and voids to varying extents.

List of Abbreviations and Symbols Used

APM: Aluminium Powder Metallurgy

AS: Advancing Side

AWS: American Welding Society

BM: Base/Bulk Material

CAB: Controlled Atmosphere Brazing

FSP: Friction Stir Processing

FSW: Friction Stir Welding

HAZ: Heat Affected Zone

LFA: Laser Flash Analysis

LPS: Liquid Phase Sintering

PM: Powder Metallurgy

RS: Retreating Side

SEM: Scanning Electron Microscope

SZ: Stir Zone

TMAZ: Thermo-mechanically Affected Zone

UBS: Ultimate Bend Strength

XRD: X-ray Diffraction

σ: Stress

Acknowledgements

The Author would like to acknowledge the Natural Sciences and Engineering Research Council of Canada (NSERC) for financial support via Discovery Grant 250034-2013. Laboratory assistance provided by colleagues at Dalhousie University (Randy Cooke, Patricia Scallion, Angus MacPherson, Mark MacDonald, and Albert Murphy) and at the University of Waterloo (Luqman Shah) is gratefully appreciated as well.

Chapter 1.0 Introduction

1.1 Aluminium Powder Metallurgy

1.1.1 Powder Production

The commercial production of aluminium powder metallurgy (PM) parts can be broken down into four generalized steps: the production and blending of the raw powder, consolidating the powder in to a green part, sintering the green part, and post sintering processing. There are many methods for the production of metal powders from raw feed stock, but when it comes to aluminium a process known as gas atomization is commonly used. While there may be differences in final implementation, the basic premise of gas atomization is relatively simple. As shown in Figure 1 a stream of molten metal is impinged upon by a high-pressure gas from a nozzle, which atomizes it into droplets as the gas expands [1].

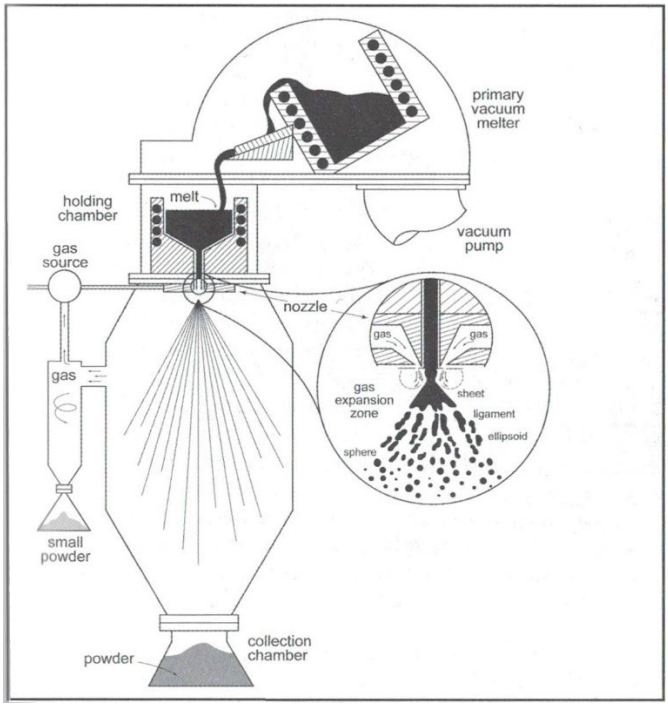

Figure 1 - Layout of a typical vertical gas atomizer [1].

The high-pressure gas used can vary depending on the metal being atomized; argon, air, and nitrogen are all common [2]. Inert gases such as argon or nitrogen may be used when oxidation of the powder is a concern, whereas air provides for an economical alternative for metals that can still be sintered when rendered into particles that are oxidized and irregular in shape. There are many factors that can be controlled to tailor the final size and morphology of the powder such as melt superheat, nozzle geometry, and gas velocity [2].

Before the powder can be compacted, it must be mixed with other powders to obtain the desired alloy chemistry. Powder manufacturers often produce metal powders as either pure elemental systems or as master alloys that are typically binary systems containing the base metal and a desired alloying addition in relatively high concentration (i.e. 5 to 50 % by weight). Appropriate combinations of such powders are then blended together to achieve a mix that maintains the final chemistry sought. During blending, lubricants are also generally added which help to reduce friction between the powder and die walls during compaction. This facilitates the attenuation of a relatively uniform green density, reduces ejection forces, and improves tool life [1].

With the powders now blended, the next step is to consolidate the mixture into the desired shape, forming what is known as a green body. In commercial aluminium PM this is generally done through uniaxial die compaction. Die compaction makes use of a hydraulic press to compact powder in a die between an upper and lower punch. Depending on part geometry the tool set may comprise multiple upper and lower punches to account for features such as vertical holes and significant changes in thickness in the pressing direction (i.e. steps), while still ensuring an appropriate degree of densification (and the uniformity thereof) during compaction. Depending on the setup of the press only one or both punches may move relative to the die during compaction; this is known as single or double action compaction, respectively. Tooling must be made from highly wear

resistant materials which also have high stiffness and compressive yield strength, owing to the abrasive nature of metal powder and the high axial loads experienced during operation. For these reasons tool steels such as A2, D2, M2, and SAE 6150, and cemented tungsten carbides grades such as C-4, C-10, C-12, and C-13 are all key materials of choice for punches and dies [2].

Compaction of the powder transpires through four distinct stages: rearrangement, localized deformation, homogeneous deformation, and bulk compression. The rearrangement stage can be thought of as the particles settling in the die. Here large spaces between particles are filled as the particles move past each other. The local deformation stage begins when the point contacts between the particles begin to deform and flatten out, allowing for improved packing. The first two stages are where rapid gains in green density are realized for relatively little compaction pressure. The next stage is marked by the entirety of the particles deforming with obvious facets developed at inter-particle contacts points. The rate of densification slows down in this stage, as the particles work harden with continued deformation and require ever increasing pressure to deform further. Bulk compression is the final stage of compaction. In this step densification slows down drastically as only small pores remain the in the structure and the particles have become fully work hardened. Owing to the significant increases in compaction pressure required for relatively minor gains in green density, a practical threshold is reached where it becomes uneconomical to pursue continued densification by compaction.

During compaction there is a significant amount of friction present; not just between the individual particles but also between the powder and the tooling. The later of these two cases is known as die wall friction and can lead to significant density gradients in the green compact, with the density decreasing away from the die walls and punch faces. Density gradients can negatively affect densification during sintering and can lead to significant sintering-induced distortion of the part if severe enough. Double action compaction can

be employed to counter this to an extent, as by compacting from both ends of the part the density gradient effectively is mirrored around the mid-depth of the part.

1.1.2 Sintering

While green bodies generally have a geometry that is close to final shape, the respective mechanical properties are wholly unsuitable for any kind of an end-use applications as the individual particles are only weakly joined together. To resolve this issue, green parts are then sintered through a prescribed thermal profile under the protection of a controlled atmosphere. Broadly speaking, sintering can be broken down in to two main types; solid-state and liquid phase. As the names imply solid state sintering occurs exclusively in the solid phase, while liquid phase sintering functions with the aid of a liquid present. Of the two, liquid phase sintering is especially important to commercial aluminium PM owing to the significantly higher diffusion rates in a liquid compared to a solid and the capillary action that a liquid phase can impart; combined, these factors frequently invoke high levels of densification in a relatively short period of time.

Sintering is the high temperature process that facilitates the bonding of individual powder particles in to a nominally solid, mechanically useful, body. This bonding is accomplished by the mass transport of atoms to areas of high vacancy concentration, which have a high surface energy, from areas of low vacancy concentration and lower surface energy. In practical terms, this is the diffusion of atoms towards the contacting surfaces between particles, which forms a solid neck with a new grain boundary formed between the previously separate particles. This reduces the ratio of surface area to volume, resulting in a reduction of the overall surface energy of the system. Qualitatively, sintering progresses in three distinct stages, beginning with the formation of necks between particles in the initial stage, but with a lack of meaningful densification. The open volume around the particles in the compact is interconnected at this point, forming a network of porosity. The intermediate stage is characterized by the rounding of pores and is where

the majority of densification occurs. Grain growth begins later in this stage and continues into the final stage. In the final stage of sintering the material has become sufficiently densified such that the pores are no longer interconnected and become trapped at grain boundaries and inside grains as grain growth progresses. When the pores break free from grain boundaries densification is effectively discontinued, since they can not effectively be removed from the material. This means that its often no longer economical to continue sintering and thus the beginning of the final stage of sintering usually marks the end of commercial sintering cycles.

The movement of atoms in solid-state sintering is accomplished through five different mass transport mechanisms which can be grouped depending on where the atoms came from to fill the neck. Surface transport mechanisms are those that move atoms on the surface of the particle towards the neck, and as such exclusively contribute to neck growth while not affecting shrinkage or densification. The diffusion of atoms along the particle surface is the most prominent surface transport mechanism, especially at lower temperature sintering. Evaporation-condensation is a less significant contributor to the surface transport of atoms due to the low vapour pressure of most metals, with the exception of some materials that have a high vapour pressure at elevated temperature (e.g. chromium) [2]. Bulk transport mechanisms move atoms from within the bulk of the material to the surface at the neck region, resulting in densification. By moving atoms from the grain boundary to the neck between two particles the geometric centers of the particles move closer together. This can be thought of as the particles “squeezing out” the pores from inside the material, as one might do with a water-soaked sponge. Owing to the previous compaction step the grain boundaries between particles and the immediately adjacent material are dislocation-rich areas. This allows for two bulk transport mechanisms to occur: grain boundary diffusion; the rapid diffusion of atoms through the grains boundaries towards the surface of the neck region, as well as plastic flow; the movement and elimination of defects in bulk lattice. When atoms diffuse through the bulk of the material it is known as volume diffusion, and this mass transport

mechanism can be categorized as either a surface or bulk mechanism depending on where the diffusing atom started.

1.1.2.1 Liquid Phase Sintering

Liquid phase sintering (LPS) exploits the significantly faster diffusion rates in a liquid phase over that of a solid phase to accelerate the sintering process. The liquid commonly comes from a eutectic reaction between two or more elements, forming a liquid with a lower melting temperature than that of the bulk material. For LPS to be used successfully there are two critical factors that must occur; the first is that the liquid phase formed must be able to wet to the bulk solid material and the second being that the bulk material must have some solubility in the liquid [1], [2]. Wetting occurs when the liquid phase is readily able to come in to contact with the solid material and spontaneously spread across the surface of the particles, owing to a low contact angle. Contact angle refers to the angle formed by the leading edge of a liquid on a solid surface and is determined by the equilibrium balance of the three surface energies of the system (solid-vapour, solid-liquid, and liquid-vapour). A contact angle less than 90° is considered to be wetting and will result in the spreading the liquid. However, values appreciably lower than this (i.e. ~0°) are preferable. In narrow gaps (as found between particles in a compact) a capillary action resulting from surface tension occurs, which acts to rapidly draw the wetting liquid into voids and pores present. The need for the solubility of the solid phase in the liquid stems from the simple fact that if atoms of the bulk can not be dissolved into the liquid then they also can not diffuse through the liquid to aid in sintering.

Like solid-state sintering, LPS happens in several distinct stages. Initially during heating, before any stages of LPS occur, a small amount of solid-state sintering takes place. The first stage of LPS is marked by the formation of the liquid phase, which causes rapid densification to occur. This densification comes about by two means; the first and most significant is the liquid flowing through and fills the open space of the pores between

particles. The second mechanism is that the liquid dissolves the minor amount interparticle bonding from the solid-state sintering that occurred during heat up, as well as the dissolution of surface asperities. By disconnecting and smoothing the particles they are freer to slide past each other and rearrange, being pulled more closely together due to the surface tension of the liquid phase. After the initial rearrangement and rapid densification the next stage known as dissolution-reprecipitation begins. Owing to the fact that the solubility of the grains is inversely proportional to their size, in this stage the smaller grains dissolve preferentially in the liquid phase, before diffusing through the liquid and precipitate on the larger grains. As this stage of LPS progresses the number of grains decreases while the average size of the remaining grains increases, at the expense of the smaller grains. The rate at which densification happens in this stage is dependant on three important factors: the solubility of the solid in the liquid, the initial particle size distribution, and the volume fraction of the liquid phase. Having a low solubility or having larger grains slows down the rate at which the solid phase can dissolve into the liquid, thus reducing the overall amount of atoms that are dissolved and diffusing through the liquid. While having too little a volume fraction of liquid has a similar limiting affect, having too much liquid (greater than approximately 35 vol.% [1]) is also detrimental, as the compact can significantly slump and deform. Some deformation is to be expected from this stage and can be corrected in post sintering operations if its not too severe.

1.1.3 Sizing

While a PM part may be placed directly into service once sintered, it is more common for some form of post sinter processing to occur; collectively known as finishing operations. These finishing steps can range from simple operations such as heat treatment to change mechanical properties, to more involved processes such as machining, which can impart features and/or dimensional tolerances that could not be produced through compaction. One operation which is especially important in commercial PM processing of aluminum alloys is known as sizing, which is a type of post-sinter deformation. Sizing is primarily performed to adjust the dimensions of the part such that they are compliant with print

specifications. While the main goal of sizing is dimensional adjustment, research has shown that it can improve other properties as well; Boland *et al.* found that aluminum PM 2324 parts showed improvements to both UTS and yield strength after sizing [3], while Judge *et al.* found that sizing had a beneficial affect on the corrosion behaviour of Alumix 123 (a PM analogue of aluminum alloy AA2014) when compared to material in the as-sintered condition [4].

1.2 Commercial Aluminium PM Alloy Systems

Within the confines of commercial PM operations, there exist a growing number of alloy chemistries that are being developed and exploited. Such alloys are frequently premised on 2xxx series wrought alloys wherein the principal alloying additions are copper and magnesium. In traditional wrought aluminium metallurgy, copper alloyed with aluminium has a significant and well-known precipitation strengthening effect. While this property is made use of in PM alloys, the addition of copper also brings about a secondary and significantly beneficial feature; the presence of a low melting temperature eutectic. As seen in Figure 2 there is a decreasing solubility of copper in pure aluminium with decreasing temperature, facilitating the precipitation strengthening effect. Also present is the existence of a eutectic point between the pure aluminium and the Al_2Cu phase which, starting at 548°C, allows a liquid to form during heating. This liquid enables the use of liquid phase sintering on green PM compacts, which can be a powerful technique for rapid densification during sintering.

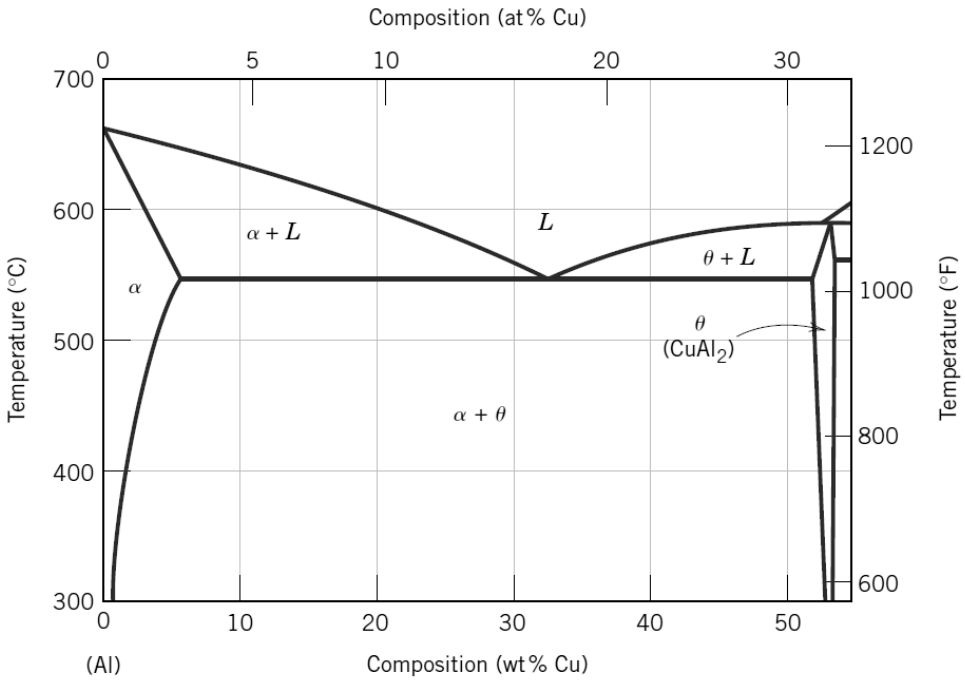

Figure 2 - The aluminium rich end of the Al-Cu Binary Phase Diagram [5].

One major downside to the use of copper is that a phenomenon known as the Kirkendall effect arises due to the significantly higher diffusivity of copper in aluminium than aluminium in copper at sintering temperatures [6]. Since the diffusion is faster in one direction than the other, and not a one-to-one atom exchange between phases, this can lead to swelling and distortion. A second problem occurs when fine copper particles are used, in that the entirety of the copper particle will rapidly diffuse in to neighbouring aluminium particles and homogenize the composition before any significant amount of liquid phase forms. When coarse particles are used this problem is mostly alleviated, as the aluminium becomes locally saturated with the solute atoms (copper) and significant quantities of liquid can form for long enough to aid in densification [7]. The Al-Cu PM system has been extensively studied, with many of the process variables that have a strong effect on the sintering response having been identified [8]. For instance, it has been shown that an atmosphere with an exceptionally low dew point is important to improve final tensile properties [9].

Magnesium has seen use with aluminium PM since some of the earliest experimental alloys, and was used in the first two commercial grades; 201AB and 601AB (Table 1) [10]. Research has shown that in the binary Al-Mg system the optimum range is 0.1-1.0 wt.% Mg, depending on the aluminium particle size [11].

Table 1 - Compositions of PM alloys 201AB and 601AB.

Alloy	Composition, wt.%				
	Cu	Mg	Si	Lubricant	Al
601AB	0.25	1	0.6	1.5	Bal.
201AB	4.4	0.5	0.8	1.5	Bal.

While it has been known that the presence of magnesium was critical to sintering aluminium PM alloys, the exact role was not fully understood until the late 1990's, when research revealed exactly how magnesium aided in the sintering process. By using synchrotron radiation X-ray photoelectron spectroscopy analysis during sintering, researchers were able to verify how magnesium behaved physically and chemically during sintering. It was shown [12] that magnesium critically acts to sequester oxygen during the sintering process in two ways:

1. Mg atoms migrate to the surface of particles and chemically reduce the alumina present, disrupting the oxide film.
2. Due to its high vapour pressure at elevated temperatures, it sublimates and reacts with any remaining oxygen in the immediate atmosphere around the particles, sequestering it and preventing the alumina layer from reforming.

Another alloying addition that is common to 2xxx aluminium PM systems is tin. Its utility lies in the fact that it can be a powerful aid during LPS. This is not done by the formation of a eutectic liquid like other alloying additions, but rather by working in conjunction with magnesium to keep the surface of the aluminium particles clean. Above 232°C tin melts and then diffuses to the surface of the particles. Once magnesium has disrupted the oxide layer, it forms a liquid film on the particles [13]. This film has a reduced surface tension, which beneficially helps by improving wetting in normally non-wetting liquids. Detrimentally however, by lowering the surface tension, the film reduces capillary pressure in normally wetting liquids which lowers the sintering stress. Importantly the film of liquid tin protects the aluminium by delaying the onset of aluminium nitride formation until later stages of sintering. This delay in AlN formation is important as it helps with pore closure. In the later stages of sintering the pores become isolated and closed off from one another. Research [9], [14] has suggested that the nitrogen gas trapped in the pores reacts with the exposed aluminium surface to form solid AlN, sequestering the nitrogen, and dropping the pressure in the pores. This decrease in pressure acts as a driving force for continued densification via pore closure.

Individually copper and magnesium both have beneficial and well-known affects on the sintering response of aluminium PM alloys, inducing LPS and disrupting the oxide layer, respectively. When used together they also have an important effect on the precipitation behaviour of the finished product, leading to improved mechanical properties of the final product. In aluminium alloys containing copper the θ-type ($CuAl_2$) precipitate is the main phase responsible for strengthening [15]. With the addition of magnesium a second precipitate known as S-type (Al_2CuMg) can form [16]. The relative abundance of the two precipitate types can have a strong affect on final properties and is primarily determined by two important factors: the ratio of copper to magnesium present and any post sintering cold working prior to heat treatment.

The ratio of Cu:Mg is important in determining whether θ-type or S-type precipitates will be present as the primary strengthening phase. In alloys where there is significantly more copper than magnesium present (i.e. those with a high ratio) the θ-type precipitate dominates owing to a low quantity of available magnesium with which to form the S-type. Correspondingly in alloys with an increased magnesium content, and thus a lower ratio, the additional magnesium allows for the formation of S-type precipitates [17]. Post sinter cold working prior to heat treatment is another important factor, as it has been found that S-type precipitates preferentially nucleate on dislocations. As previously mentioned, a cold working step (in the form of a post sinter sizing operation) is a conveniently common stage in the commercial aluminium PM process, especially when working with Al-Cu-Mg PM alloys. When combined with an alloy chemistry that maintains an adequately low Cu:Mg ratio a sizing step promotes a refined distribution of precipitates in the final PM part.

These two factors can be seen in research undertaken by *Boland et al.*, where in they were successfully able to produce a novel PM alloy (dubbed PM 2324; Al-4.5Cu-1.5Mg) which had improved mechanical properties compared to a commercial PM alloy (AC 2014; Al-4.5Cu-0.6Mg), without compromising commercially important die compaction behaviour or sintering response [3].

1.3 Existing PM Aluminium Alloys

The first aluminum PM alloy to be used on a commercial level was AC2014. The alloy was effectively a PM version of the existing AA2014 wrought alloy, but with minor compositional changes (i.e. the removal of manganese) to improve compactability [18]. In the automotive sector a desire for improved fuel efficiency via decreased vehicle weight led to an increased use of aluminium in place of the existing ferrous alloys. Initially being used in the manufacture of camshaft bearing caps in the 1990's, PM AC2014 replaced the existing expensive and time-consuming die casting method. Since the die cast blanks

required significant machining after casting, the net-shape PM approach was advantageous in comparison as it only required a simple line boring operation [19].

The successful application of PM AC2014 led to the development of additional APM alloys that are now employed in commercial applications. Examples include PM2324, PM2618, and TC2000, as well as Alumix grades 231 and 431D. Unlike earlier PM alloys which were often simply powdered versions of existing wrought alloys, PM2324 is an alloy developed from, and as an improvement on, the older PM alloy AC2014. Compositionally it is very similar but instead of just having good final properties it has been modified to work well during all stages of the aluminium powder metallurgy (APM) process. The increased magnesium content of PM2324 compared to AC2014 (1.5 vs. 0.6 wt.%, respectively) not only resulted in a marked improvement in densification during sintering, but also realized a significant improvement in mechanical properties. In standard APM processing it is common practice to size (effectively a cold forging process) parts after sintering to improve dimensional tolerances of the final part. The additional Mg content when combined with the sizing step results in a change in the precipitation behaviour during later heat treatment, promoting a refined distribution of precipitates on the dislocations induced during the sizing process [3], [20].

The system PM2618 is another commercial PM alloy with rising popularity. While aluminium alloys are not generally considered to be high temperature materials, PM2618 was developed with thermal stability in mind. Effectively a PM counterpart to wrought AA2618, PM2618 fills the niche in the PM aluminium alloys that have good mechanical properties and are able to retain good properties even after prolonged exposure to elevated temperatures. Cooke *et al.* determined that even after prolonged exposure at the relatively high temperature (for aluminium alloys) of 260°C the alloy had comparable properties to it's wrought counterpart [21].

TC2000 (Al-1Mg-1.5Sn) is a PM alloy that was developed to be a light weight, economical, and highly thermally conductive material ideal for applications (such as heat sinks) which could benefit from the APM process [22]. Heatsinks are ideally made from either pure copper or aluminium owing to their high thermal conductivity. Neither pure metal is an ideal candidate for automotive use as copper is relatively heavy and expensive compared to aluminium, while pure aluminium is extremely difficult to sinter. While alloying aluminium makes it easier to sinter, it also negatively affects its thermal conductivity. TC2000 addresses these issues in that it is an alloy of mostly aluminium while still sintering to near full theoretical density (> 99%), and maintains a high thermal conductivity in excess of 200 W/mK [23], [24].

Alumix 231 (Al-15Si-2.5Cu-0.5Mg) is a commercial hypereutectic aluminium-silicon PM alloy. Aluminium-silicon alloys are traditionally the realm of castings where their high silicon content improves melt fluidity [25]. These alloys have several advantages over other aluminium alloys such as high wear resistance and low thermal expansion, in addition to high strength and good thermal stability. Cast Al-Si alloys are susceptible to the formation of relatively large crystals of primary silicon, which negatively affects mechanical properties. PM processing of Al-Si alloys overcomes these problems, as the rapid solidification during powder atomization not only limits the size of the primary silicon crystals but also allow for significantly higher solid solubilities to be obtained [26].

Alumix 431D is a commercial PM blend that exists as a counterpart to the high strength wrought alloy AA7075. Research into this alloy by LaDelpha *et al.* showed that this alloy sintered well (reaching approximately 99% of its theoretical density) and behaved comparably to its wrought counterpart in terms of ageing behaviour and thermal stability. The mechanical properties showed some deviances as it was found that while the yield strength and hardness were inline with the wrought alloy, the ultimate tensile strength, stiffness, and ductility were inferior [27].

Chapter 2.0 Joining Technologies for Aluminium Alloys

2.1 Brazing

Brazing is a relatively high temperature joining process where two or more pieces of metal are joined using a filler metal. Two pieces are closely fitted together and heated while a filler metal is added to the joint. The filler metal melts at a lower temperature and wets to the bulk material, being pulled into the very fine gap between the contacting surfaces of the joint by capillary action. For metals that are sensitive to oxidation at high temperatures (such as aluminium) a flux is used which is a substance that melts and covers the surfaces of the joint, providing a chemical cleaning action and preventing oxidation. Flux assists in the wetting of the filler metal and is often critical to the brazing process. The important difference between brazing and welding is that in brazing the bulk material does not melt, such that welding related problems such as solidification cracking are avoided.

2.1.1 Filler Metals

When brazing, an ideal filler metal is one that has the best balance of desirable properties, as it is often impossible to perfectly match the properties of the bulk metal to the filler metal. Some of the critical properties considered when choosing a filler metal include: wetting of the metal being brazed, complete melting below the solidus temperature of the substrate metal, mechanical and physical properties that match the material being brazed, material availability, etc.. Unlike some materials which use a dissimilar family of alloys for filler metals (i.e. copper alloys for the brazing of ferrous alloys), the filler metals used when brazing aluminium are all aluminium-based Al-Si alloys from the 4XXX series. Table 2 gives the chemistries of several commonly utilized filler materials.

Table 2 - Compositions of standardized aluminium filler metals. Nominal values for alloying additions are bolded. [28]

UNS Number A9xxxx	AWS Designation	Composition, wt.%								
		Si	Cu	Fe	Mn	Mg	Zn	Bi	Other, Each	Other, Total
4343	BAlSi-2	**7.5**	0.25	0.8	0.1	-	0.2	-	0.05	0.15
4145	BAlSi-3	**10**	**4**	0.8	0.15	0.15	0.2	-	0.05	0.15
4047	BAlSi-4	**12**	0.3	0.8	0.15	0.1	0.2	-	0.05	0.15
4045	BAlSi-5	**10**	0.3	0.8	0.05	0.05	0.1	-	0.05	0.15
4004	BAlSi-7	**9.75**	0.25	0.8	0.1	**1.5**	0.2	-	0.05	0.15
4147	BAlSi-9	**12**	0.25	0.8	0.1	**0.3**	0.2	-	0.05	0.15
4104	BAlSi-11	**9.75**	0.25	0.8	0.1	**1.5**	0.2	**0.11**	0.05	0.15

Al-Si alloy compositions are chosen to make use of the low temperatures and narrow melting range near the eutectic point, and as such all feature a high silicon content. A low melting temperature is desirable from both economic and production stand points. Lower temperature processing equipment is less expensive to purchase and maintain, and lower temperatures are easier to work with. A narrow range between the solidus and liquidus temperatures of the filler alloy is desirable as it reduces the chance of a skull of metal being left behind where the filler metal was positioned during assembly. A skull forms as a result of a process known as liquation wherein there is inhomogeneous melting of the filler metal due to slow heating through its melting range [28], [29]. Some of the metal is left behind while the portion that has melted is wicked away in to the joint. In aluminium-silicon alloys this skull can be formed from the secondary silicon phase if the heating rate is too low, or from remnants of the oxide layer if it was not adequately reduced by the flux.

2.1.2 Fluxes

2.1.2.1 Corrosive Fluxes

There are two types of fluxes for brazing aluminium; corrosive and inert [29], [30]. Corrosive fluxes consist of various alkali-chloride salts mixed with small amounts of alkali-fluorides. The chloride salts (Na/K/LiCl) act as a carrier, while the fluorides (NaF and AlF_3) perform the fluxing reaction [28], reducing the aluminium oxide layer. Corrosive fluxes do not entirely decompose during the brazing process, and the post-braze residue left on the assemblies is hygroscopic. This causes the residue to collect moisture out of its environment, trapping it against the aluminium, and potentially causing corrosion of the brazed assemblies. For this reason, it is extremely important that all flux residue is thoroughly cleaned from the assemblies; a process which is both time consuming while adding cost and complexity to production. If exposed to moisture while molten, corrosive fluxes will react to produce hydrofluoric acid which instantly turns to vapour at the temperatures at which brazing is preformed. Not only does this pose a serious hazard to workers and equipment, but the vapours need to be neutralized before being released to the atmosphere. Due to these problems corrosive fluxes have fallen out of use in favour of inert fluxes, which are easier and safer to work with.

2.1.2.2 Inert Fluxes

Inert fluxes were first introduced under the NOCOLOK® branding by the company Solvay Fluor GmbH, and have since become the *de facto* industry standard flux for industrial aluminium brazing. Inert fluxes consist of a mix of potassium fluoroaluminate compounds, with a general formula of $K_{1\text{-}3}AlF_{4\text{-}6}$ [31]. One of the most important factors of inert flux is that the post-braze residue is not hygroscopic and does not cause corrosion if left on the assemblies after brazing. Not only does this save time by removing a cleaning step from the production process, but it also reduces costs as there is no longer an aqueous effluent stream from the wash water to be dealt with [29]. Much like corrosive fluxes, as both

contain fluorine compounds, inert fluxes can produce hydrofluoric acid vapours if exposed to moisture while molten.

Along with the baseline NOCOLOK flux, several derivatives have been produced with modified behaviour. While the post braze residue is inert from a corrosion standpoint, it is slightly soluble in water. One variant (NOCOLOK Li) of the regular flux is produced which contains an addition of lithium fluoroaluminate (Li_3AlF_6), which results in reduced solubility of the post braze residue. This variety was designed for use in places where water pools, specifically for use in the HVAC industry where brazed assemblies may be in contact with stagnant water. It was found that "…a flux with lower solubility helped meet the requirements of the HVAC industry's corrosion test requirements" [32]. A second derivative of interest is one which contains a small amount (up to 2 wt.%) of additional cesium fluoroaluminate ($CsAlF_4$) flux (NOCOLOK Cs). This addition helps the baseline flux handle aluminium alloys with an increased magnesium content (maximum of 0.8 wt.%, up from 0.5 wt.% Mg). With the baseline flux magnesium causes unwanted side-reactions which consume the flux before it can fully reduce the aluminium oxide layer. The addition of cesium was found to act as a chemical buffer, sequestering the excess magnesium (forming $CsMgF_3$ and/or $Cs_4Mg_3F_{10}$ [31]) before it can consume the flux, improving the overall fluxing behaviour such that the aluminium oxide layer is fully reduced.

2.1.3 Dip Brazing

Dip brazing, or more specifically chemical-bath dip brazing, is a brazing process whereby assemblies are submerged in a bath of molten salt and flux. It has historically made up the bulk of aluminium brazing production before controlled atmosphere brazing was developed [33]. By completely immersing assemblies not only is air thoroughly excluded from reacting with molten filler metal, but it also facilitates uniform heating of the assembly, which helps prevent distortion caused by uneven heating. Immersion heating results in faster heating rates (4-5x) than those commonly found in furnace heating [28],

which also facilitates the formation of many joints rapidly; a factor that aids economical brazing of complex multi-jointed assemblies such as radiators, as it helps to reduce processing time.

The molten salt-flux mix used with dip brazing is the corrosive type, as dip brazing pre-dates the introduction inert fluxes. The exact ratios, and which chloride and fluoride salts are used vary between manufactures and are often proprietary knowledge; they are however, chosen to give the best combination of fluxing ability, melting range, fluidity, reduced salt dragout with the assemblies, and improve the resulting surface finish [28]. Prior to being dipped the assemblies have to be preheated to within (typically) 55°C of the brazing temperature [28]. This preheating step can be accomplished with a dedicated furnace or by simply suspending the fixtured assemblies over the molten salt-flux bath. The preheat step is necessary for several reasons: to reduce thermal distortion, remove all moisture from the assembly, and to prevent the molten salt from freezing on contact with the assemblies, which would insulate them and prevent adequate heating. It is critical with dip brazing that all moisture is removed prior to dipping as not only does it react with the flux to produce hydrofluoric acid vapours, but it will also flash to steam when submerged, which can cause splattering of the molten salt-flux [28], endangering workers.

Because corrosive salt-fluxes are used, brazed assemblies have to be thoroughly cleaned after undergoing brazing. Since cleaning has to be extremely thorough, more complex assemblies are accordingly harder to clean. Assembly geometry needs to be carefully considered when dip brazing; blind holes and joints (see Figure 3) can trap air and salt, leading to incomplete joint formation and corrosion. At a minimum, cleaning involves washing in boiling or agitated hot (82°C) water[28]; chemicals (i.e. strong acids) [34] can be added to the cleaning bath to help with residue removal and improve the final finish of the brazed assemblies.

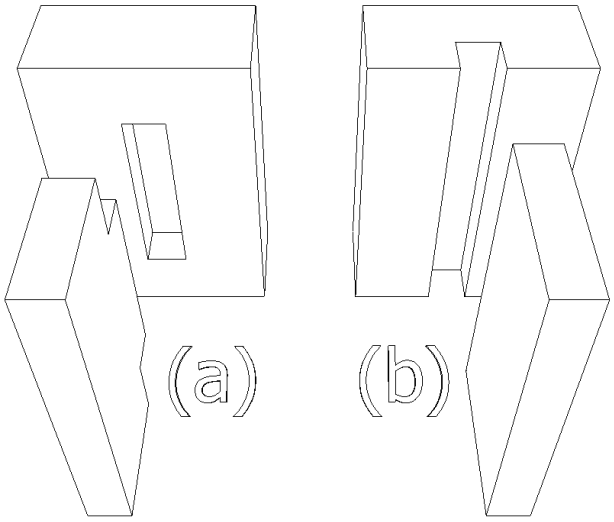

Figure 3 - Blind joint (a) vs. through joint (b).

2.1.4 Torch Brazing

Torch brazing (or flame brazing) is preformed in open air, wherein the joint is heated directly by use of an oxy-fuel flame. Hence, heavy flux loadings are used to compensate for the uncontrolled atmosphere. Torch brazing is practical for low volume production of assemblies which have few joints. Since every joint in an assembly is made one at a time torch brazing rapidly becomes impractical as a joining technique, from both a time and economic perspective, to braze assemblies with a multitude of joints (i.e. radiators). The set up used for torch brazing can be as simple and low cost as a trained operator wielding a torch, up to the complexities (and increased costs) of a fully automated mechanized brazing machine.

When torch brazed manually, the consistency of joint quality can become a concern. Precise temperature control is critical to a well formed joint; a challenging prospect when using a torch to heat a joint. Since the melting temperatures of the bulk metal and the filler metal (both being some type of aluminium alloy) are very close, a small mistake with the torch could melt through an assembly. The relative closeness of the melting

temperatures means that there is practically no room for the use of superheating to improve filler metal fluidity to help fill a joint [29]. The problem of temperatures becomes further exacerbated when attempting to braze together pieces with significant mass differences, i.e. a thin fin to a thick tube or solid block, as the heating time becomes uneconomically long [28]. Adding further complexity to the situation is the strong affinity the aluminium-silicon filler metal has for the aluminium bulk metal, which it dissolves to some extent while in contact with the molten filler metal [35].

2.1.5 Furnace Brazing

2.1.5.1 Vacuum Brazing

Vacuum brazing takes place in specially designed, sealed, brazing furnaces under a high vacuum atmosphere. The furnaces used can be designed for batch-wise operation or for semi-continuous throughput. The former consists simply of a single sealed furnace chamber whereas the latter (as pictured in Figure 4) is more complex, consisting of multiple sealed and heated chambers connected by vacuum-tight internal doors. Each chamber is plumbed and operated separately, so as to achieve the desired atmosphere and heating/cooling requirements for each stage of the process.

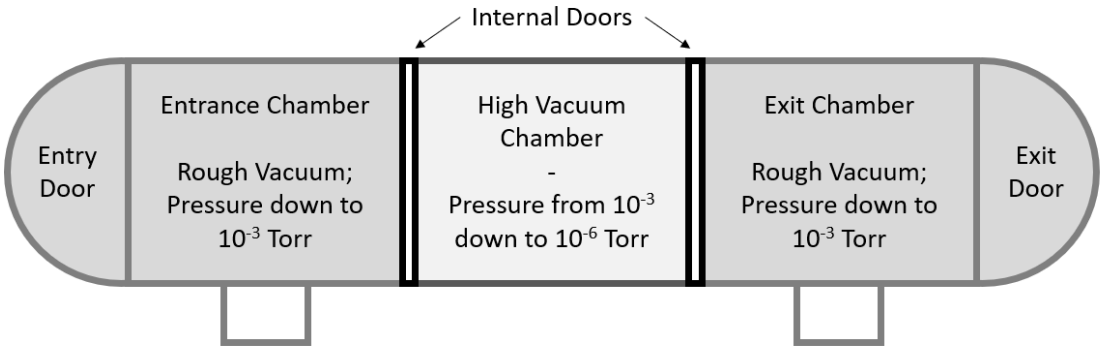

Figure 4 - Schematic of a semi-continuous vacuum furnace. [28], [29]

Owing to the effective absence of oxygen in the process atmosphere, a dedicated flux is no longer mandatory as a small concentration of magnesium in the alloy and/or filler metal is typically sufficient. Magnesium reacts with the aluminium oxide layer to reduce it to magnesium oxide (MgO) and/or small quantities of spinel ($MgAl_2O_4$) [28], [29]. Since the vacuum will never be perfect, the magnesium will also react with any oxygen left in the furnace [36], helping to purify the atmosphere further. To this extent, magnesium may be added to a tray in the furnace for the explicit purpose of improving the atmosphere in the furnace [28] via a gettering effect. While an effective method, vacuum brazing is slow and an expensive process to operate. In addition, the magnesium oxide dust produced during brazing poses a health hazard to workers who can accidently inhale it, resulting in a condition known as “metal fume fever” [37].

2.1.5.2 Controlled Atmosphere Brazing

Controlled atmosphere brazing (CAB) is a process where assemblies are joined under a high purity nitrogen atmosphere, in a belt fed continuous furnace. Since its inception in the early 1980’s [29], [38], [39] the process has seen wide spread adoption to the point of becoming the industry leading method for brazing industrial quantities of complex and multi-jointed assemblies, such as radiators. Figure 5 gives examples of brazed aluminium components commonly found in automotive use that are ideal candidates for CAB manufacturing.

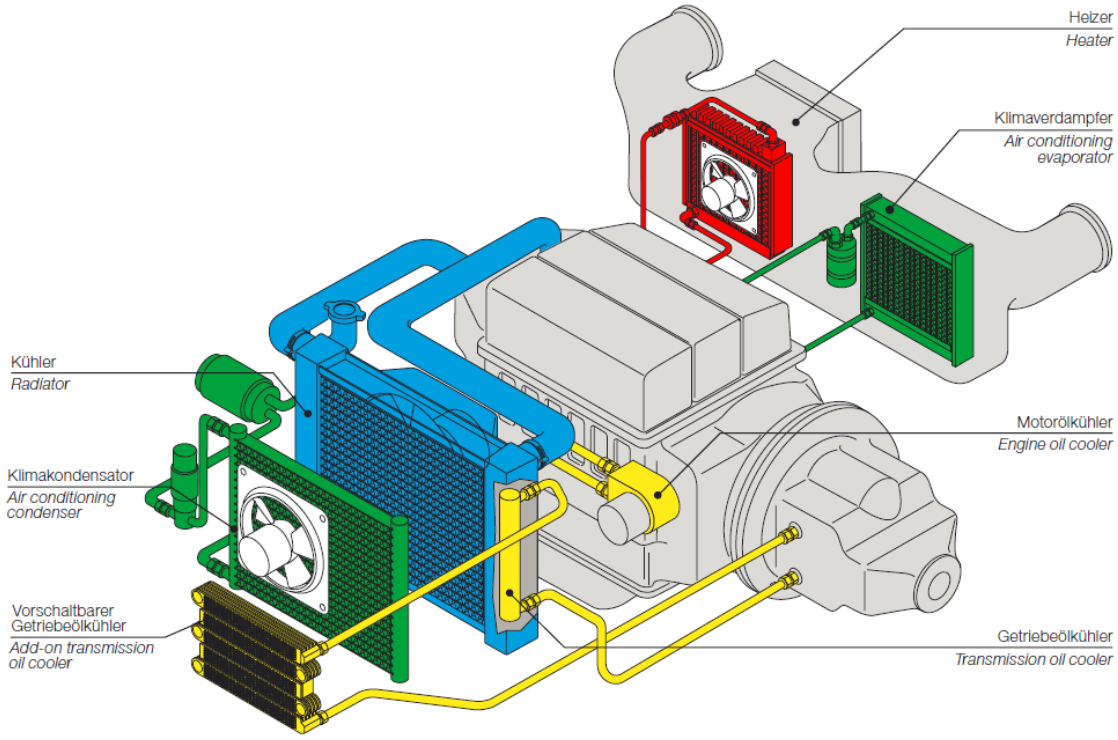

Figure 5 - Common automotive assemblies made via controlled atmosphere brazing [40].

The process is sometimes also called the NOCOLOK method as it was developed in conjunction with, and makes use of, the inert fluxes originally introduced as the range of NOCOLOK products made by Solvay Fluor GmbH. Controlled atmosphere brazing has several key benefits over other industrial brazing processes, specifically related to the throughput, atmosphere, and flux use. Since the furnaces used in CAB are belt fed and open on either end, they are ideal for large production volumes. While CAB furnaces operate under a controlled atmosphere of pure nitrogen, they also operate at near-atmospheric pressure, which simplifies equipment and reduces costs. As nitrogen gas is constantly being pumped into the furnace it operates under a very slight positive pressure which removes the need for seals around moving parts, entrances, and exits. Not having seals to wear out or expensive vacuum pumps to maintain lowers costs and improves up-time. Since the CAB process makes use of inert flux, the benefits associated with inert fluxes carry over; most importantly that brazed assemblies don't require an additional

cleaning step after brazing. Compared to vacuum brazing, for the production of vehicle radiators, costs are reduced and productivity is increased by some 30% [30].

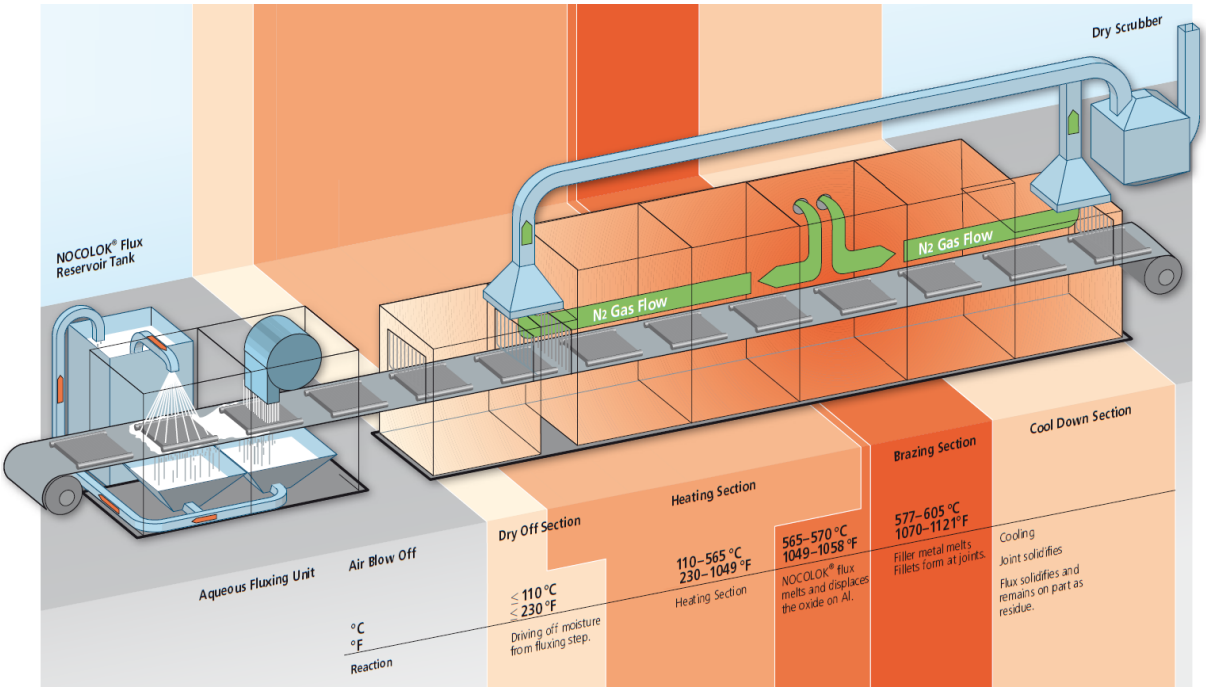

Figure 6 - The "NOCOLOK Method" [40]

Figure 6 shows a general layout of the CAB process. The first stage is fluxing of the fixtured assemblies, where the flux in the form of an aqueous suspension is applied. There are several methods of application such as spraying (shown in the figure), flooding (passing through a waterfall of flux suspension), and electrostatic application (preformed with dry flux powder). Extra flux suspension is removed by a stream of air, which also helps to dry the applied flux. The next stage is a drying step, where assemblies are heated to remove all moisture from the flux. Moisture contaminates the pure nitrogen atmosphere of the furnace and reacts with the flux to produce hydrofluoric acid vapours. From this point in the process onwards, all steps occur under an atmosphere of dry, high purity nitrogen.

Dried assemblies then enter the first heating zone of the furnace where they are preheated to within a few degrees of the flux melting temperature. Assemblies are then ramped to the fluxing temperature and subsequently to the brazing temperature where they are typically held for 30 to 120s prior to cooling. Since the flux has limited useful lifespan once molten, it is important that the assemblies are thoroughly preheated such that the flux can melt all at once, then be rapidly followed by brazing temperatures so that the filler metal has a clean surface to wet.

2.2 Friction Stir Welding

Friction stir welding (FSW) is a relatively novel joining process for metallic materials. The process uses a rotating non-consumable tool which is plunged into the material and then moved along the joint. This induces intense frictional heating and local softening, which allows the material to be plastically deformed and stirred around the tool. As the tool is moved along the joint material is stirred from in front of the tool to behind it, completely backfilling the path. When appropriate processing parameters are used the volume stirred by the tool is highly homogenized and free of voids. Importantly, FSW process is classified as a solid-state process as the frictional heating is sufficiently intense enough to soften the material, it is not adequate to induce melting. The absence of a liquid phase permits the joining of materials previously considered to be impractical or outright “unweldable” through traditional fusion welding such as 2xxx, 7xxx, and 8xxx series aluminium alloys [41]. Compared to fusion welding, the reduced heating leads to less strain and warping in the material, while the lack of liquid formation means that problems such as solidification cracking do not occur.

The fundamental geometry of the FSW tool consists of two parts: the pin and the shoulder. The pin is the part that is plunged into the material and does the stirring. It is positioned on the end of a larger diameter cylinder which forms the shoulder. The primary purpose of the shoulder is to contain and push down the material displaced by the pin,

preventing it from being displaced outward and around the sides of the tool. The entire tool is angled backwards at a very small tilt angle (generally < 2°), such that the shoulder on the leading side of the tool is slightly above the surface of the material being joined, but not so much that the trailing edge displaces a significant trough of material. The geometrical features of the pin can vary significantly with processing parameters and application, ranging from simple cylinders with threading and facets to complex spiraling flutes and even off-centre pins.

The microstructure of a friction stir weld can be broken down in to the four regions shown in Figure 7, which are distinguishable by the varying amount of heating and deformation the material has experienced. In the center of the weld is the stir zone (SZ) or nugget; this is material that has been directly stirred by the tool. This region has seen the most intense heating and deformation and has generally undergone dynamic recrystallization, prompting the presence of fine equiaxed grains. The intense stirring action in this region also breaks up any large clusters of secondary phase particles and/or precipitates, leaving a fine distribution(s) thereof amongst the newly recrystallized grains. The thermo-mechanically affected zone (TMAZ) is the region immediately adjacent to the stir zone on either side. It consists of material that has seen significant heating and deformation, but not enough to have undergone recrystallization. Accordingly, it has the general appearance of grains of the base material that have been heavily deformed and stretched. Past the TMAZ lies the heat affected zone (HAZ), which comprises material that has seen elevated temperatures but has not experienced deformation. Beyond the HAZ is the bulk material (BM) which has not experienced any meaningful changes from the FSW process.

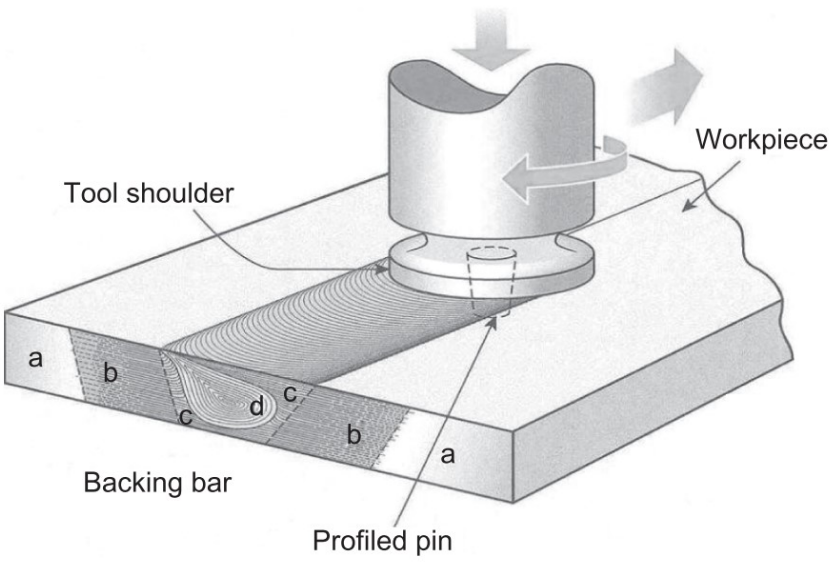

Figure 7 - Generalized schematic of the FSW process and microstructural regions: (a) BM, (b) HAZ, (c) TMAZ, and (d) SZ. [42]

Since its initial development in 1991 FSW has seen significant adoption in the aerospace industry as well as in various transportation focused industries including automotive, marine, and railway. Rocket and aircraft manufacturers continuously seek to reduce the weight of their vehicles without sacrificing strength, something which is accomplished by implementing high strength aluminium alloys. These alloys however frequently prove to be troublesome to weld by traditional means, often requiring careful thermal control before, during, and after welding to prevent defects such as porosity and cracking. FSW has thus proven to be a very appealing solution to the problems faced by the aerospace industry as the entirely solid-state process avoids the conditions necessary for these defects to form. By 2001 NASA had adopted the use of FSW in manufacturing the final version of the space shuttle external fuel tank. Known as the Super Lightweight Tank, it used over 200 m of friction stir welds on a new Al 2195 structure, replacing the older Al 2090 structure and shaving roughly 3175 kg off its mass

[43], [44]. Boeing implemented a FSW specific design of the first stage tank of their Delta IV rocket, which resulted in a 60% cost saving and a manufacturing time reduction from 23 to 6 days [45]. Eclipse Aviation was the first commercial aviation company to implement FSW in civilian aircraft. Making extensive use of FSW in the manufacture of their Eclipse 500 small business jet Eclipse was able to replace over 7000 rivets with 263 friction stir welds [41]. The process was used to join lap joints of Al 2024 and Al 7075 in both homogeneous and dissimilar alloy welds [46].

FSW has seen adoption in various transportation-based industries including rail, shipbuilding, and automotive for joining sections of aluminium extrusion and sheeting. FSW is particularly well suited to these applications as the reduced heating compared to traditional welding leads to less distortion of the final part; something which is critical when working with thin extrusions and long welds. Hitachi and Bombardier have both implemented FSW in the manufacture of passenger trains where it is primarily used to join aluminium extrusions and large body panels [47], with some welds having lengths upwards of 25 m [41]. The automotive industry has increasingly sought to implement high strength aluminium alloys in vehicles due to a desire to reduce weight without reducing passenger safety. Owing to its highly automated nature and consistent weld quality compared to traditional fusion welding, FSW has shown itself to be a viable method to increase the use of aluminium in vehicles. Nearly all aluminium components used in cars can be stir welded, be it important structural features such as rollover beams and crash boxes, or power train components such as engine blocks, drive shafts, and axels [48]. Ford notably made use of FSW to attach the central transmission tunnel made from an aluminium extrusion in the first-generation Ford GT, which added important stiffness to the aluminium body structure [49].

The shipbuilding industry has taken up FSW not only for the production of lightweight ship structures, but also for equipment used aboard ships. The Scandinavian countries were

some of the earliest adopters of FSW for use in maritime industries. Hollow deep freezer panels have been made by Sapa of Sweden from aluminium extrusions for use on fishing boats to rapidly freeze fresh fish [45]. Hydro Marine Aluminium of Norway have been using FSW since the early 2000's to produce prefabricated panels for high speed ferryboats from extrusions, which thanks to the low distortion aspect of FSW are able to fit together with a high degree of dimensional accuracy, leading to improved mechanical alignment and production times [48].

The presence of any kind of pore or crack, no matter how small, poses a significant hygienic concern in food processing and handling equipment. The food industry, which makes extensive use of aluminium, has found use for FSW when manufacturing equipment since the lack of weld pool precludes the formation of these types of defects. Riftec, a German supplier of FSW services has been producing freeze drying trays and hand guards for meat slicing machines made from stir welded aluminium. Production has been on the order of several thousand units annually since the mid 2000's [45].

Chapter 3.0 Mechanical Testing of Joined Assemblies

3.1 Tensile Testing

Tensile testing is an established technique for determining mechanical properties of materials. It generally involves pulling a specimen in a uniaxial fashion under increasing load until a certain condition is met; usually when failure occurs. Shown below in Figure 8, the typical geometry of specimen used for tensile testing often has a gauge section with a reduced cross section, where stress (and thus deformation and failure) is focused during testing. Testing of a jointed specimen in tension typically involves a butt joint with the plane of the joint perpendicular to the direction of pulling, i.e. the joint cuts through the cross section of the gauge length.

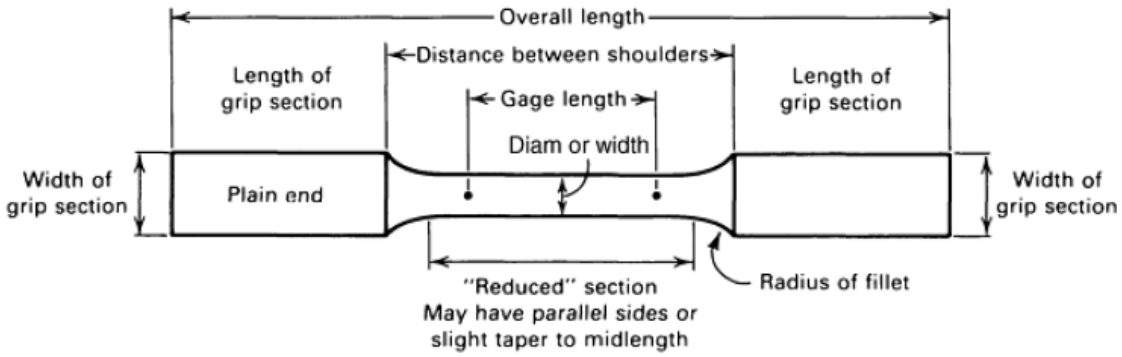

Figure 8 - Profile of a typical tensile specimen. [50]

Tensile testing is, mechanically speaking, a simple test to perform. The equipment needed to do so consists of a load frame with data logging capabilities - equipment which is commonly found in materials research laboratories. Tensile testing has the additional benefit of loading the entire cross section of the joint simultaneously.

While it does have its benefits, tensile testing is not without its detractions. Should the failure of the specimen occur not at the joint but elsewhere, i.e. in the bulk metal, then

the properties of the joint cannot be assessed beyond knowing that the strength of the joint in tension is apparently higher than that of the bulk material or that the joining process has weakened the surrounding material. Failure in the specimen away from the joint can also occur if there are any defects in the test specimen (from poor sample preparation or naturally occurring), which can act as stress risers. As tensile specimen tend to require tight and consistent tolerances, and in some cases need to be cylindrical, they require machining on a mill or lathe. Regardless of whether this is done by a skilled operator or by computer control both options can present an increased cost-per-specimen, depending on the tolerance required. Additionally, tensile tests are sensitive to misalignment of the testing fixture which can lead to unwanted bending moments and the introduction of errant data.

3.1.1 Tensile Specimen Geometries – AWS D17.3/D17.3M:2016 Standard

The American Welding Society (AWS), in standard D17.3M:2016 gives several tensile test specimen geometries. This includes specimen suitable to be made from flat plate and pipe sections with a thickness of 25 mm or less, as well as a specimen with a machined cylindrical cross section. When the thickness of the base material exceeds 25 mm several specimen of equal size should be made.

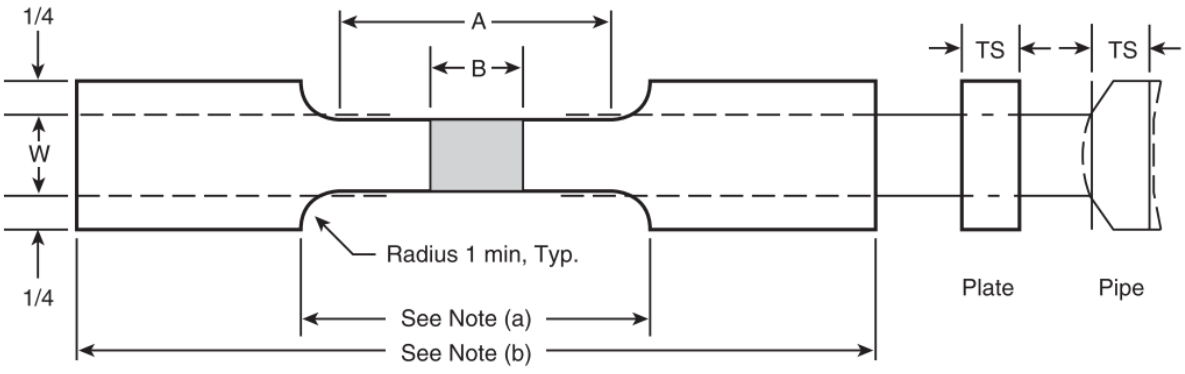

Figure 9 - AWS D17.3/D17.3M:2016 tensile specimen geometry for plate and pipe material [51].

Figure 9 gives the geometry suitable for specimen made from plate and pipe sections (full details in Appendix A, Figure 36). Section “B” represents the FSW joint, which should be located in the middle of the reduced section. The standard specifies that the reduced section should be cut by machining or grinding and that its length “A” should be the width of the joint plus 13 mm or a total of 57 mm, which ever is greater. The width “W” of the reduced section should be 19 mm for both plate and pipe derived samples, except in cases where the pipe outer diameter is less than 76 mm then the width should be 13 mm.

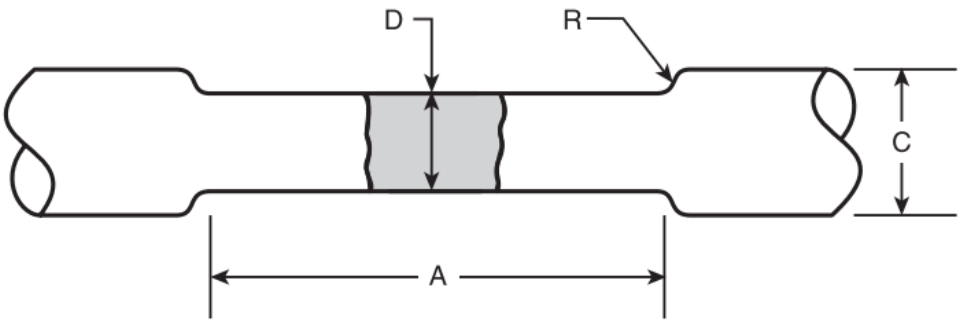

Figure 10 - AWS D17.3/D17.3M:2016 tensile specimen geometry with a machined cylindrical cross section [51].

Figure 10 gives the geometry for a cylindrical specimen that can be used when test equipment necessitates a round sample or when using a large sample with sufficient material available to be machined round. As with the previous geometry, the FSW joint (indicated in grey) should be located in the middle of the reduced section, with the overall length of the reduced section “A” no less than the width of the weld joint plus two diameters. The specimen end diameter “C” and shoulder radius “R” are dependant on the reduced section diameter “D”, for which the standard (Appendix A, Figure 37) lays out four acceptable diameters ranging from 4.77 mm (0.188 in) to 12.7 mm (0.5 in).

3.2 Bend Testing

Bend testing is a format commonly employed to evaluate the ductility and quality of a welded joint. It is frequently employed as a qualitative, pass/fail, style of test that can be performed on a shop floor as opposed to a dedicated testing lab. While the tooling and specimen geometry used can vary, the general procedure involves bending a butt welded test coupon to a predetermined angle and then inspecting the joint for defects such as cracking [50]. Specimen frequently take the form of a rectangular bar with the weld joint located in the center. Bend tests can be broadly divided in to two types: guided and unguided (or freeform). In the former, deformation of the sample is controlled as force is applied at the joint through the use of supports or a jig, as is commonly found in three-point bending set ups. In the latter, there is no control over deformation during the test; force is only applied at the ends of the sample which are simply brought together and the material is allowed to deform naturally. Since bending loads one side of a sample in tension and the other in compression it is important to consider sample orientation with respect to the weld when testing; a defect in the weld root is unlikely to be revealed if the top surface (the face) of the weld is put in tension.

3.2.1 Bend Specimen and Fixture Geometry – ISO 5173:2009 Standard

The ISO 5173:2009 standard lays out simple specimen geometry (Figure 11) for testing the weld face, root, and the full weld depth (side bending) of plate and pipe material. In all cases the specimen is a flat rectangular bar with a maximum thickness in the bending plane ("t_s") of 10 mm. If the bulk material has a thickness ("t") greater than 10 mm but less than 30 mm, the standard allows for material to be machined off the side opposite the testing surface. When testing material greater than 30 mm thick several specimen at consecutive depths should be tested. Minimum specimen length "L_t" is as required by the testing equipment. The minimum specimen width "b" should be four times the thickness for plate derived samples and 8 mm (but no greater than 40 mm) for pipe derived samples.

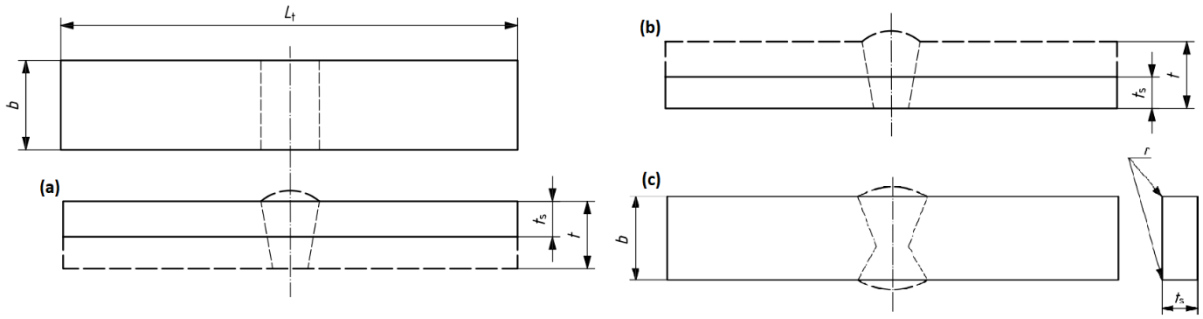

Figure 11 - ISO 5173:2009 Specimen geometry for transverse face (a), root (b), and side (c) bending [52].

Also given in the ISO 5173:2009 standard are three example geometries for guided bending fixtures: a three-point bend fixture, a U-type jig, and a roller. The three-point bend fixture (Figure 12) makes for a good general-purpose apparatus, usable with a large range of materials and sample dimensions. The sample rests on the two stationary bottom rollers while the top one applies load to the weld joint, deflecting it downwards. The test is considered complete when the test specimen is sufficiently bent such that it can pass between the support rollers.

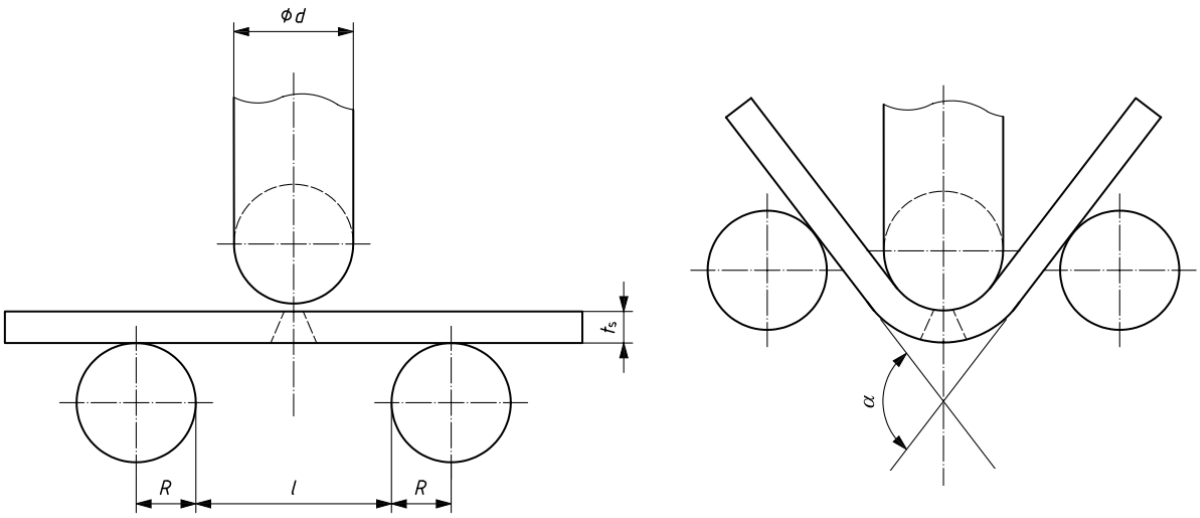

Figure 12 - ISO 5173:2009 Three-point bending fixture geometry, showing before and after bending arrangment [52].

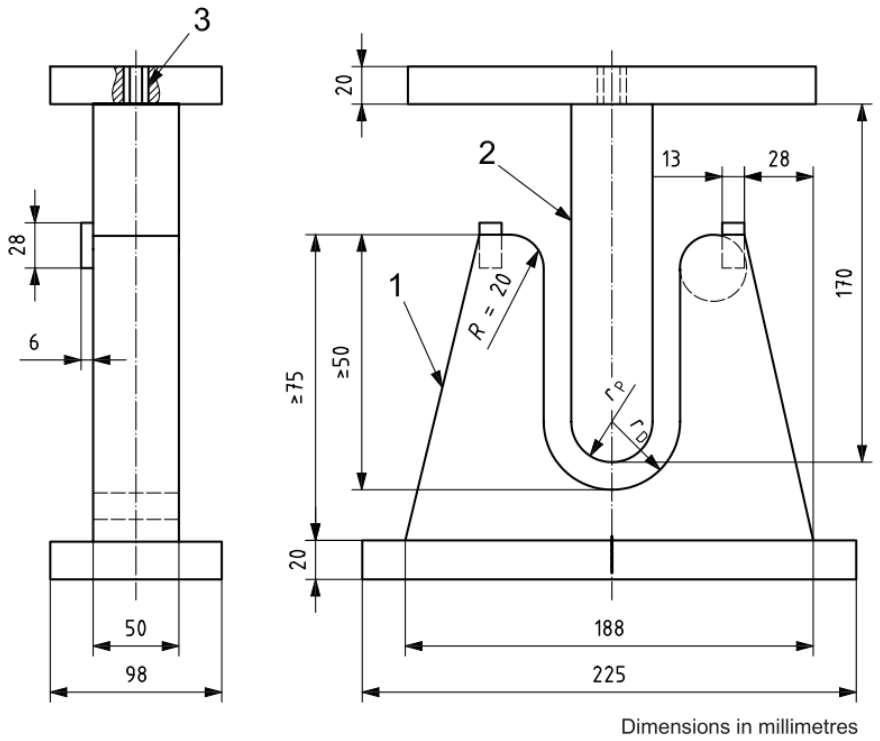

Figure 13 - ISO 5173:2009 U-type jig [52].

Figure 13 gives the dimensions for a U-type bending jig, primarily intended for the bend testing of thin samples. Effectively behaving the same as the three-point bending set up, the test sample rests across the top of the die (“1”) where it is then pushed down into the U-shaped channel by the plunger (“2”). The radius of the plunger (“r_P”) and the die (“r_D”) are determined by the thickness of the sample; for 10 mm thick samples the plunger and die radius’ are 20 mm and 32 mm respectively. For thinner samples the plunger radius should be two times the sample thickness and the die radius should be equal to the plunger radius plus the sample thickness and an additional 2 mm. The test is completed when the sample has deflected sufficiently that a 3 mm wire can not be inserted between the sample and the bottom fixture.

The third type of bend tester given in the standard is a roller type, intended for material with a relatively high degree of elongation such as aluminium or in cases where metals

with dissimilar strengths have been joined. The tester behaves similarly to a commercial pipe bender; one end of the specimen is clamped in place while an outer roller bends the sample in an arc around an inner former. For samples which have a parent material with a high degree of elongation (≥20%) the diameter of the former is simply four times the sample thickness. For samples with lower parent metal maximum elongation (i.e. <20%) the diameter is based on a function of sample thickness and parent metal elongation, with the former increasing in diameter as the maximum elongation decreases. The test is finished when the outer roller has moved in a 180° arc from its starting point.

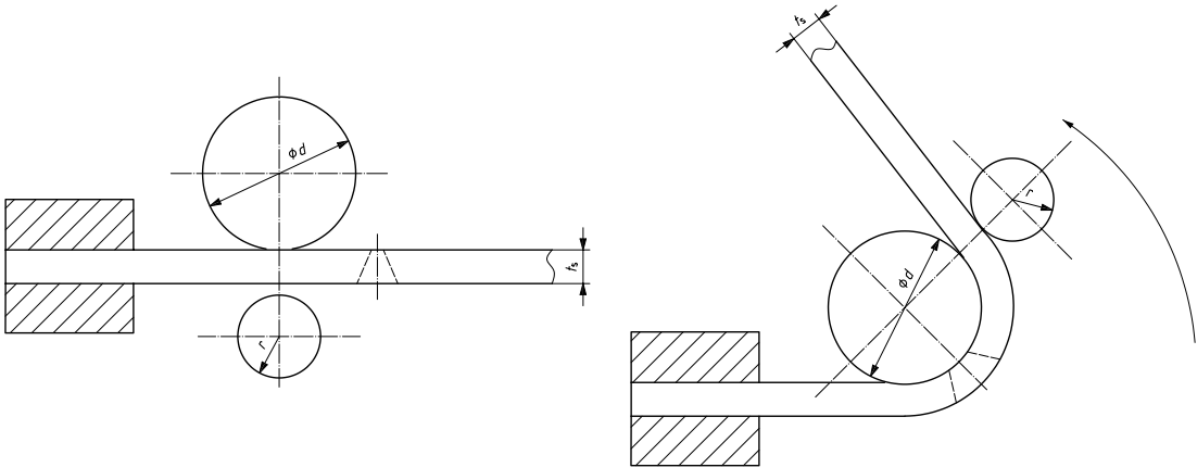

Figure 14 - ISO 5173:2009 Roller type bend testing apparatus [52].

3.3 Fatigue Testing

Fatigue testing is an important form of mechanical testing used to determine the properties and behaviour of materials subject to cyclic loading. Fatigue is the cyclic loading of a material or joint that causes detrimental and permanent changes eventually leading to failure, even at stresses below the yield point of the material [53]. How many cycles a material or joint can be loaded to at a specified stress before failure is known as fatigue life and is critical knowledge for the design of mechanical parts and structures. This data is frequently plotted as a S-N curve, which plots the cyclic stress against the number of

cycles to failure. To generate the fatigue life data, representative test coupons are subject to cyclic loading until either failure occurs or the runout criteria is met; usually when the sample endures a predetermined number of cycles.

Specimen loading is generally done in one of three basic modes: uniaxial, plane bending, and rotating-beam [50]. Uniaxial, or direct axial loading is performed in a manner similar to a conventional tensile test, except that the specimen is rapidly cycled between a loaded and unloaded state, with modern systems using closed loop computer controlled servo-hydraulics for precision control. Plane bending is performed using the same type of equipment, with the key distinction being that the sample is loaded using a three- or four-point bending fixture. This allows for the direct testing of a welded joint, as the peak load can be positioned directly on one part of a sample, unlike in axial loading which loads the entire length of the specimen. Rotating-beam fatigue testing bends a sample while simultaneously rotating it, which causes the material to cycle between the maximum tensile and compressive stresses.

It is important to note that with both plane bending and rotating beam testing, only the material at the sample's surface experiences the maximum stress, whereas with uniaxial testing the entire cross section is loaded to the maximum stress. Careful consideration must be taken in sample preparation as it is critical that the surface of a test sample be free of any unintentional features that act as stress risers, such as scratches, machining marks, or even indents from testing equipment grips; all of which can lead to premature specimen failure.

3.3.1 ISO/TR 14345 - Guidance for Fatigue Testing of Welded Components

Owing to the vast number of existing and ever novel welding geometries, configurations, and methods, no one standard would be sufficiently comprehensive for all situations. The

ISO technical report 14345 offers guidance and best practises for the production of test specimen and fatigue testing of welded joints, allowing users to be more comprehensive when validating designs.

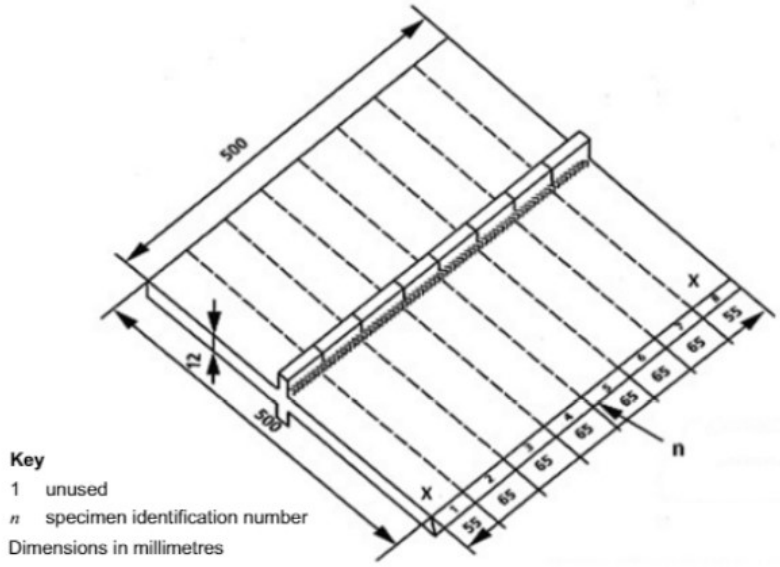

Figure 15 - ISO/TR 14345 Example of a welded panel for the extraction of several identical test specimen [54].

In situations where many identical specimen are needed, such as in the creation of a S-N curve, it is recommended that they be extracted from a single larger panel, as demonstrated in Figure 15. By discarding the end segments where the welds start and stop, this technique allows for the production of many specimen from a single larger fillet or butt weld which helps to maintain a consistent joint quality across all specimen. This technique has its drawbacks however, as it is only suitable for instances where the axis of fatigue loading is perpendicular to the weld axis. In instances were the loading axis runs parallel to the weld axis it becomes necessary to produce individual specimen. When testing samples in fatigue it is important to ensure that failure occurs at the intended location (i.e. the weld) as opposed to an arbitrary location in the bulk material, especially in situations where the welded feature has relatively high fatigue strength.

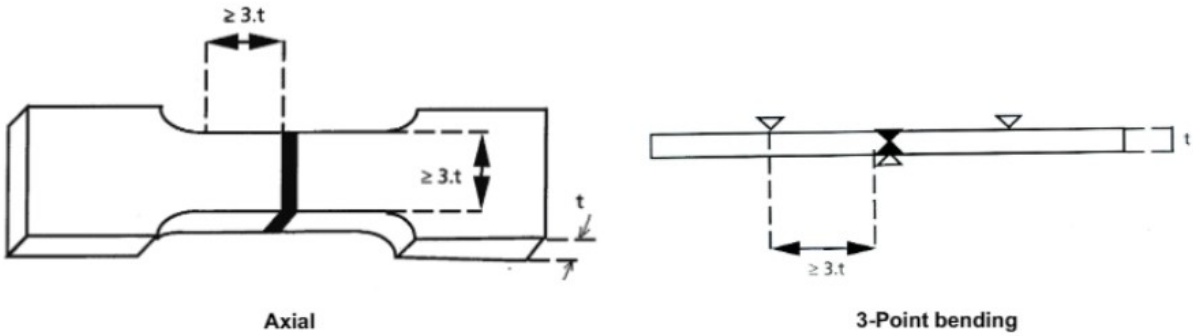

Figure 16 - ISO/TR 14345 Dimensional recommendation for samples used in axial and plane bending [54].

Figure 16 gives recommended general dimensions for samples used in axial and bending loading. The axially loaded specimen features a reduced section with the weld in the middle as it is important that any deformation or notching caused by the wedge grips do not affect the failure location. Likewise the 3-point bending sample specifies a minimum distance for the supports from the weld so as to ensure there is no accidental failure caused by indentation from the supports.

Chapter 4.0 Research Objectives

The objective of this research was to determine the response of two commercial aluminium PM alloys to FSW. Due to the PM nature of the materials investigated and how little existing literature there is on the FSW of PM materials, specific interest was placed on how varying the processing parameters affected the resulting microstructure as well as the mechanical properties in bending under static and fatigue loading. While there are many variables involved in the FSW process, tool rotation speed and traverse rate were the primary focus of the research effort.

Chapter 5.0 Friction Stir Processing of Aluminium Powder Metallurgy Alloy PM2618

The research, results, and discussion of the following paper was completed by James Adye. The co-authors acted as reviewers and editors.

J.R. Adye[1], I.W. Donaldson[2], A.P. Gerlich[3], D.P. Bishop[1*]

1-Dalhousie University, Dept of Mechanical Engineering, 1360 Barrington Street, Halifax, NS, Canada

2-GKN Sinter Metals, Advanced Engineering, 1670 Opdyke Court, Auburn Hills, MI, USA

3-University of Waterloo, Department of Mechanical & Mechatronics Engineering, 200 University Avenue West, Waterloo, ON, Canada

* Corresponding Author: Paul.Bishop@dal.ca, Ph. 1.902.494.1520

Abstract

Friction stir welding (FSW) is a novel solid-state process known to facilitate the joining of materials that exhibit a poor response to conventional fusion welding technologies. Certain aluminium alloys in the 2xxx series are prime examples as their use in welded structures is desirable, but typically avoided in light of their acute sensitivity to solidification cracking. To date, the majority of FSW research on these alloys has involved wrought products, leaving a clear void in the understanding of how those produced through aluminum powder metallurgy (APM) alloys respond. To address this shortfall, the response of a commercially relevant APM alloy denoted as PM2618 (Al-2.3Cu-1.6Mg-1Fe-1Ni-0.5Sn) to FSW was investigated in this study. The rotation speed and traverse rate of the tool were the principal process variables considered. A variety of processing parameter combinations were found to produce defect-free welds when inspected through X-ray techniques coupled with metallographic inspection of polished cross sections. The stirred material was found to have a highly refined microstructure, showing an increase in hardness but without any apparent change to the nominal phase composition. Bend testing revealed significant improvements as a result of FSW. These included a near doubling of ductility, an average increase in yield strength in bending of 33%, and a 35% improvement in UBS. Bending fatigue behaviour was also investigated, with averaged gains of 27% measured relative to the as-sintered base material.

5.1 Introduction

Friction stir welding (FSW) is a relatively new technology for the joining of metallic components. It is novel in that it facilitates the joining of materials with an absence of melting, filler metals, or fluxes. The technique uses a rotating tool to generate heat due to friction as it is pressed against the metals of the joint. The materials plastically deform around the rotating tool, which is then moved along the joint. Material is thereby stirred from the front to the rear of the tool so as to fill the gap formed by lateral tool motion [55]. The geometry of the tool consists of a pin (that is depressed into the material), on the end of a larger cylinder which forms a shoulder. This method allows for the joining of materials and alloys where traditional techniques such as fusion welding would be inappropriate or otherwise challenging/impractical, such as 2xxx, 7xxx, and 8xxx series aluminium alloys [41].

FSW sees frequent use in the aerospace sector as it is often used to join large panels of vehicle skins and fuel vessel walls. NASA was an early adopter of the technology and by 2001, the space shuttle external fuel tank contained over 200 m of friction stir welds [43]. The Eclipse 500 was the first commercial aircraft to use FSW, replacing over 7000 fasteners with 263 stir welds [41]. FSW sees use in other sectors as well, with the railway and automotive industries making increased use of the technology. Both Hitachi and Bombardier Transportation make use of FSW in the manufacture of passenger trains, for joining aluminium extrusions and panels [47]. Several automotive companies have utilized FSW in the manufacture of cars and aftermarket parts. Notably, Ford implemented FSW to join aluminium extrusions when fabricating the central transmission tunnel of the first-generation Ford GT, while Tower Automotive utilized FSW to join extrusions in the manufacture of suspension links for Lincoln limousines [49].

The 2xxx series aluminium alloys are prime candidates for FSW as many alloys in this series suffer from acute sensitivity to solidification cracking during fusion welding [56]. These

alloys are heat treatable, being primarily alloyed with copper and magnesium and maintain a high strength to weight ratio. When properly heat treated, 2xxx series aluminium alloys can have properties approaching or even surpassing those of some low carbon steels [57] making them a popular choice for aerospace applications. Accordingly, a substantial body of research has been completed on the FSW of wrought 2xxx series aluminium alloys. For instance, Benavides *et al.* [58] examined the affects of starting temperature on the microstructure of FSW Al2024. The behaviour of precipitates in the heat affected zone of stirred Al2024-T351 was analyzed and correlated with the resulting hardness by Jones *et al.* [59]. Numerous researchers have examined the fatigue behaviour of stir welded joints produced in wrought 2xxx series alloys, including Al2219-T62 [60], Al2024-T4 [61], and Al2198-T8 [62].

As aluminum-based FSW studies have largely focussed on wrought systems, there exists a distinct technological gap in the understanding of its applicability to others such as those processed through APM concepts. High volume commercialization of APM commenced in the 1990's at which time AC2014 (Al-4.5-0.9Si-0.6Mg) [63], [18] was utilized in the production of camshaft bearing caps. Success in this application ushered in a sustained period of alloy development, and ultimately, an appreciable expansion in the scope of 2xxx APM alloys available for commercial exploitation. One, denoted as PM2324, is chemically similar to AC2014 but was specifically designed for APM processing. In this sense, it offered heightened densification during sintering and the capacity to maximize the benefits accrued during post-sinter sizing (cold working) by controlling precipitation behaviour [3], [20]. Another (PM2618) was developed as a counterpart to wrought 2618 so as to address a lack of APM alloys that not only had good mechanical properties, but also demonstrated thermal stability [21]. APM has also been leveraged to develop and commercialize metal matrix composites. Key examples include recent work by Sweet *et al.* wherein AlN particulates were utilized as the strengthening feature [64]. Systems such as these are now exploited in the production of planetary reaction carriers mass produced by General Motors. As the world's first lightweight carrier, this ground-breaking

component ultimately won the Grand Prize award in the Metal Powder Industries Federation "2018 PM Design Excellence Awards Competition" [65]. The objective of this research was to commence a preliminary investigation of FSW as it relates to modern APM alloy systems. Samples of alloy PM2618 (Al-2.3Cu-1.6Mg-1Fe-1Ni-0.5Sn) were prepared for this purpose, subjected to friction stir processing/welding, and then characterized in detail.

5.2 Materials

The alloy used in this research was PM2618. The targeted and actual (measured) compositions of the samples utilized are shown in Table 3. The raw powder mixture was premised on a base aluminum powder that was prealloyed with 1 weight % each of iron and nickel. This was mixed with elemental powders of magnesium and tin, as well as master alloy powders as the sources of copper (Al-50Cu weight%) and silicon (Al-12Si weight%) so as to achieve the targeted composition defined in Table 3. The measured results were obtained by inductively coupled plasma optical emission spectrometry and agree with the nominal values targeted. The average particle size of each powder employed is presented in Table 4. The magnesium powder was produced by Tangshan Weihao Magnesium Powder Co. Ltd., Qian'an, China whereas all others were produced by Kymera International, Velden, Germany. To aid in compaction behaviour, the powder blend also contained 1.5 weight % of admixed lubricant powder (Licowax C, Clariant Corporation).

Table 3 - Nominal and measured compositions of alloy PM2618 (weight %).

Alloy	Al	Cu	Mg	Fe	Ni	Si	Sn
Target	Balance	2.3	1.6	1	1	0.2	0.5
Measured	Balance	2.33	1.49	1.17	0.99	0.20	0.54

Table 4 - Base powder D_{50} values.

Powder	Al-1Fe-1Ni	Al-50Cu	Al-12Si	Mg	Sn
D_{50} [μm]	77	31	33	31	4

5.3 Methodology

All test samples were produced using a conventional press-and-sinter approach, followed by machining to final dimensions. Raw powders were blended in a Turbula shaker mixer for 40 minutes after each addition. The first mixing step consisted of the base aluminum and the two master alloy powders being blended. To this, the two elemental powders were then mixed in, and finally the Licowax C was added for a total mixing time of 120 minutes. The powder blend was die pressed via uniaxial compaction in a floating die setup situated between compression platens in an Instron 5594-200HVL hydraulic load frame. All green compacts were flat rectangular bars (92.2 x 20.6 x 6.4 mm) and were pressed at 200MPa. Sintering was performed in a three-zone Lindberg/Blue M tube furnace under a flow of high purity (5N) nitrogen. The atmosphere was conditioned through an evacuation (10^{-2} torr) + N_2 backfill sequence that was repeated twice prior to heating. Temperature was monitored constantly using a type K thermocouple that was positioned within 1 cm of the sintering compacts. Green bars were first de-lubricated for 20 minutes at 400°C, then sintered at 610°C for 20 minutes. The bars were then cooled from 610°C to room temperature via gas quenching in a water jacketed section of the furnace. All sintered bars were then machined to the final specimen geometry (88 x 19 x 5 mm).

Initially, singular bars were friction stir processed (FSP) along their centerline at four different spindle speeds (710, 900, 1120, and 1400 RPM) and at four different traverse speeds (63, 90, 125, and 180 mm/min), for a total of 16 unique processing parameter combinations. Here, individual bars were clamped in a vice along their long edge with the center of the bar supported underneath via a 12.7 mm wide machinist's parallel bar. The

stirring tool was made of H13 tool steel and consisted of a flat shoulder with a threaded, tapered, pin with three flats. The FSP operation was performed using a Jafo milling machine with a 7.5 HP (5.6 kW) spindle, operating in displacement mode. When joining pairs of machined bars, FSW was completed using a butt joint configuration. Here, bar pairs were firmly clamped together in a vice with the joint supported underneath via a 12.7 mm wide machinist's parallel bar. Samples were stir welded in accordance with the parameter combinations given in Table 5 with six duplicates produced for each set.

Table 5 - Processing parameter combinations implemented in FSW trials.

	Parameter Combinations			
Spindle Speed [RPM]	710	900	1120	1400
Traverse Speed [mm/min]	63	90	125	180

When needed, select specimens were heat treated to a T6 state. Here, samples were solutionized at 530°C for two hours in a Lindberg/Blue M box furnace, water quenched, and then aged at 200°C for 20 hours in a Heratherm mechanical convection oven. Stir welded samples for 3-point bend testing (static and fatigue) were sectioned perpendicular to the weld track using a Struers Minitom wafering precision saw. Saw cut faces were machined square and to a fixed cross section of 12 x 5 mm (width x thickness). Before testing, the machined faces and bottom were lightly sanded with 600 grit SiC sandpaper to remove burrs and machining marks. Samples were then tested in a 3-point bending configuration, with a span of 24.7 mm across the bottom two pins of a MTS 642 bend fixture installed in an Instron Model 1332 servo-hydraulic frame. In some instances, specimens were statically loaded to fracture. In others, test bars were subjected to fatigue loading (25Hz, R=0.1) following the staircase method to determine fatigue strength as described in MPIF Standard 56 [66]. Runout was set at 10^6 cycles and a step size of 10 MPa was utilized.

Microhardness testing was performed with a Clemex CMT system to generate hardness maps of the cross sectioned surfaces before and after T6 heat treatment. A micro Vickers indenter was employed with a 200 gf load. The indent pattern was centered on the stir zone (SZ) and consisted of a grid of 53 points horizontal by 14 points vertical, with a 300 µm spacing between points in both directions. This pattern was centered on the middle of the SZ, such that the complete weld was probed. Optical microscopy was performed using a Keyence VK-X1000 laser confocal microscope while electron microscopy was conducted with a Hitachi model S-4700 field emission scanning electron microscope (SEM) operated at 10 kV and with a beam current of 10 mA. In both instances, the specimen of interest was mounted in conductive Bakelite and then ground/polished using a Struers Tegramin auto polisher. Prior to polishing samples were ground flat on 320 grit SiC sandpaper for 45 seconds. Polishing was performed using a series of progressively finer grit suspensions: first a 9 µm diamond suspension (Struers DiaPro Allegro/Largo) for 7 minutes, followed by a 3 µm diamond suspension (Struers DiaPro Dac) for 2 minutes and 40 seconds. The final polishing step was done with a 0.25 µm colloidal silica suspension (Struers OP-S) for 1 minute and 30 seconds, with a continuous water flush of the polishing pad occurring during the last 20 seconds to remove the slightly alkaline suspension. Etching of samples was performed by immersion for 6-7 seconds in Keller's Reagent (etchant No.3 from ASTM E407-07). X-ray diffraction (XRD) was performed using a Bruker D8 Advance system, utilizing copper Kα X-rays generated using an accelerating voltage of 40 kV and a tube current of 40 mA. Samples for XRD were made by first filing a solid sample then collecting and using the filings that passed through a 45µm screen. All FSP/FSW samples were inspected for defects using X-ray radiography. A Sperry SPX X-ray tube system operated at 90 kV and 3 mA was utilized for this purpose.

5.4 Results and Discussion

5.4.1 Aluminum Powder Metallurgy (APM) Processing

Test specimens were produced through an APM press-and-sinter manner of processing. To ensure that these were compliant with past studies [21], the densities of select bars were measured in the green (as-compacted) and sintered states. As shown in Table 6, a strong agreement between the current and prior works was observed. This indicated that the starting powder mixture exhibited an appropriate response to PM processing. Most notable was the fact that a nearly pore-free sintered product was readily obtained.

Table 6 - Data on select attributes quantified during the APM production of PM2618 test specimens. Prior work data sourced from Cooke *et al.* [21].

	Measured	Prior Work
Green Density [g/cm^3]	2.427	2.438
	± 0.004	±0.001
Green Percent Dense	87.7%	88.1%
	± 0.2%	±0.1%
Sintered Density [g/cm^3]	2.749	2.747
	± 0.003	± 0.002
Sintered Percent Dense	99.3%	99.3%
	± 0.1%	± 0.1%

Images of the starting (as-sintered) microstructure of the PM2618 specimens are shown in Figure 17. These confirmed the density measurements shown in Table 6 as the presence of residual porosity was highly sporadic. When observed, pores were small and isolated consistent with the attenuation of a high sinter quality. Microstructurally, the alloy was primarily composed of nominally equiaxed grains confirmed to be α-aluminium by means of XRD (Figure 18). Average grain size was determined using the intercept method and found to be approximately 37+/-6 µm. From Figure 17 and Figure 18, it was also confirmed that the alloy was multi-phased. Visually discrete secondary phases were present inside the grains and along the grain boundaries. Those located at grain interiors appeared as small, discrete dark spots and were especially apparent when the sample was etched

(Figure 17 (b)). While most grains contained a fine dispersion of these features some appeared completely devoid of them. When situated along grain boundaries, the secondary phase was dark grey and existed in a comparatively concentrated format. These resided along nearly all boundaries to some extent and were particularly prominent at points where three or more grain boundaries intercepted. Many small peaks believed to stem from the secondary phases were observed via XRD. While most were matched with phases in the software database, some remained unidentified. Such data indicated that the principal secondary phases present were most likely $Al_9Fe_{0.7}Ni_{1.3}$, Al_7Cu_2Fe, and Al_2CuMg.

5.4.2 Friction Stir Processed (FSP) Specimens

Having confirmed that the APM test coupons were consistent with prior data on the PM2618 system, research then transitioned into studies on the effects of FSP. Here, the tool was passed along the longitudinal center line of singular test bars under various combinations of tool rotation and traverse speeds. The first means of evaluation was non-destructive inspection for internal voids and flaws. Such defects appeared as dark, irregularly shaped regions in the X-ray images and when present, the associated combination of processing parameters was deemed to be unacceptable. This metric was only applied to the homogenous segment of the track (i.e. if a defect appeared within the circular boundary encompassing the point of tool withdrawal it was not counted). In some cases, these defects were fragmented into localized flaws while in others they existed as seemingly continuous voids that effectively traversed the full length of the FSP track. Exemplary radiographs that illustrate the various nature/extent of defects encountered are shown in Figure 19 while a summary of the complete X-ray findings is given in Table 7. Visually, nearly all of the FSP specimens showed no outward indications that they were defective. However, it is apparent from Table 7, that some 40% contained readily detectable sub-surface flaws. The fact that these were hidden was likely due to the trailing side of the tool's shoulder closing off the top of the defects as it passed over them.

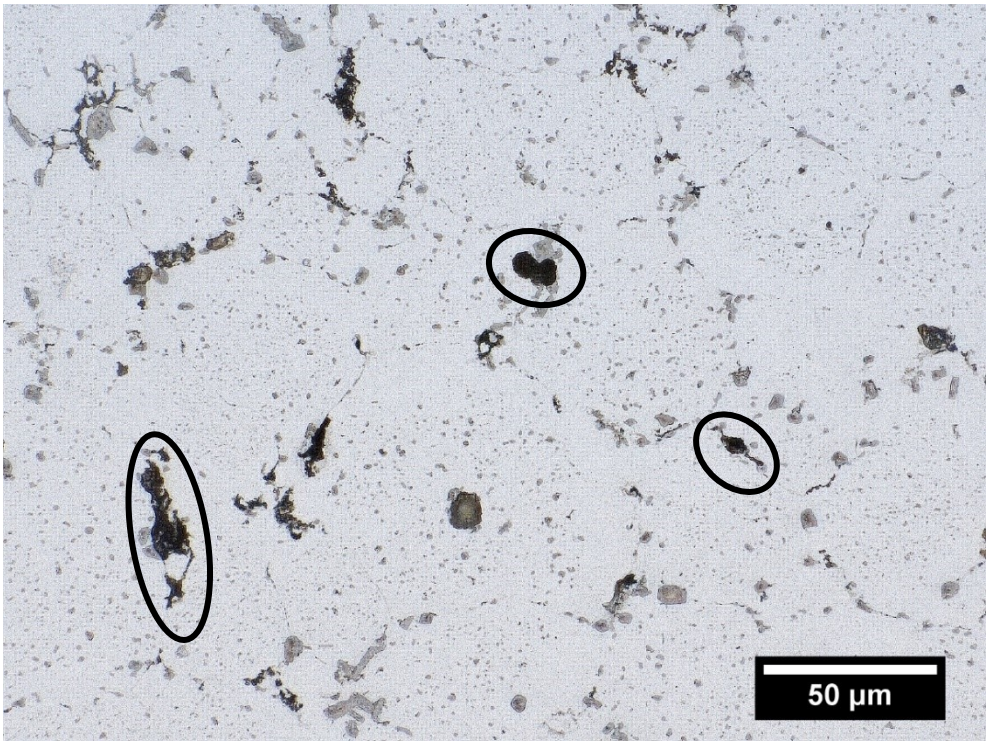

(a)

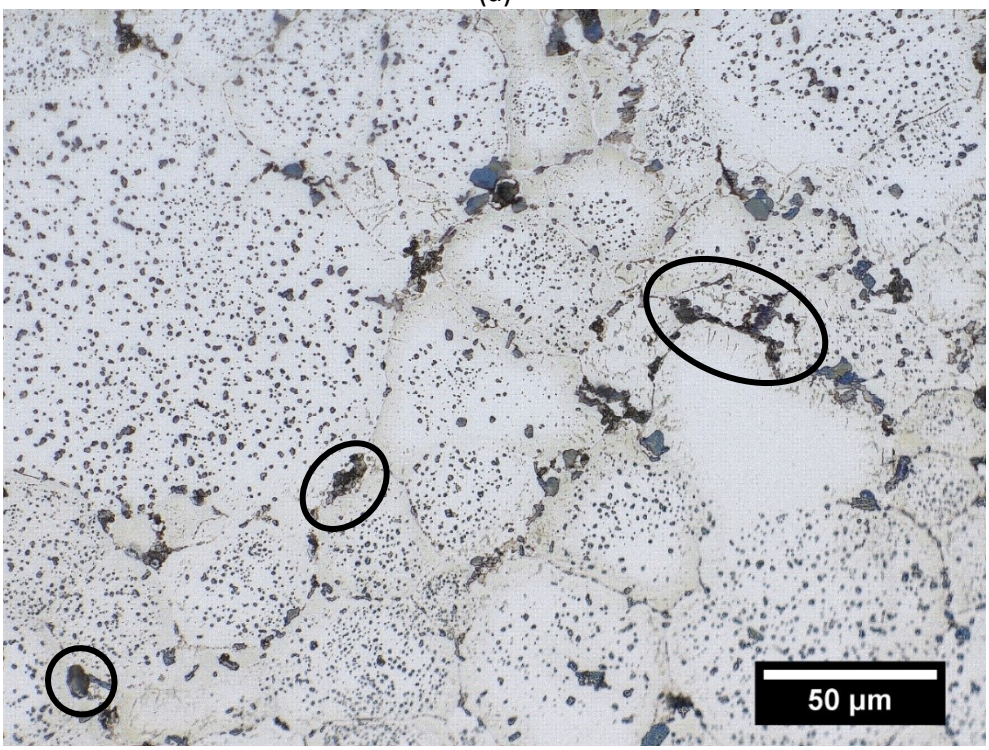

(b)

Figure 17 - Microstructure of PM2618-T1 as observed through optical microscopy. (a) unetched and (b) etched. Encircled regions indicate typical residual porosity seen in samples.

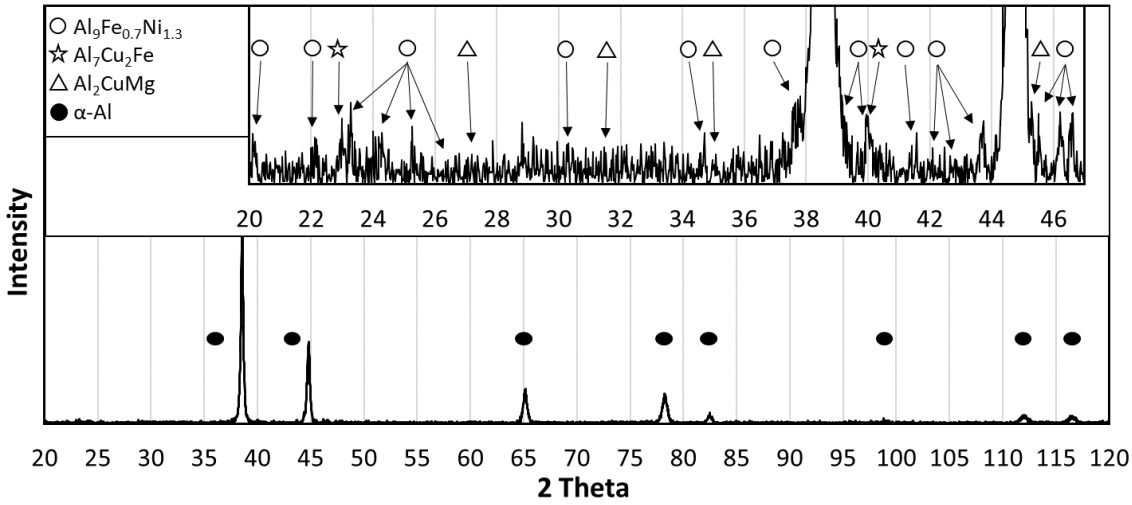

Figure 18 - X-ray diffraction pattern recorded from a PM2618-T1 test specimen. Inset trace is a magnified view that enhances the secondary low angle peaks observed.

The samples that showed the most obvious defects were generally those that utilized processing parameter combinations that were on the contrasting extremes of the testing range; i.e. high tool rotational speed paired with a low traverse speed or low tool rotational speed paired with a high traverse speed (e.g. 63 mm min^{-1} @ 1400 RPM). Conversely samples which were defect-free tended to follow "like-like" processing parameter pairings, i.e. high tool rotational speed paired with a high traverse speed. When the parameter combinations were quantified as tool advancement per revolution, it was found that successful parameter pairings generally fell in a range around 0.07 to 0.13 mm/revolution while defective pairings where typically found above and below this range. However, this was by no means a definitive trend as several exceptions were also noted.

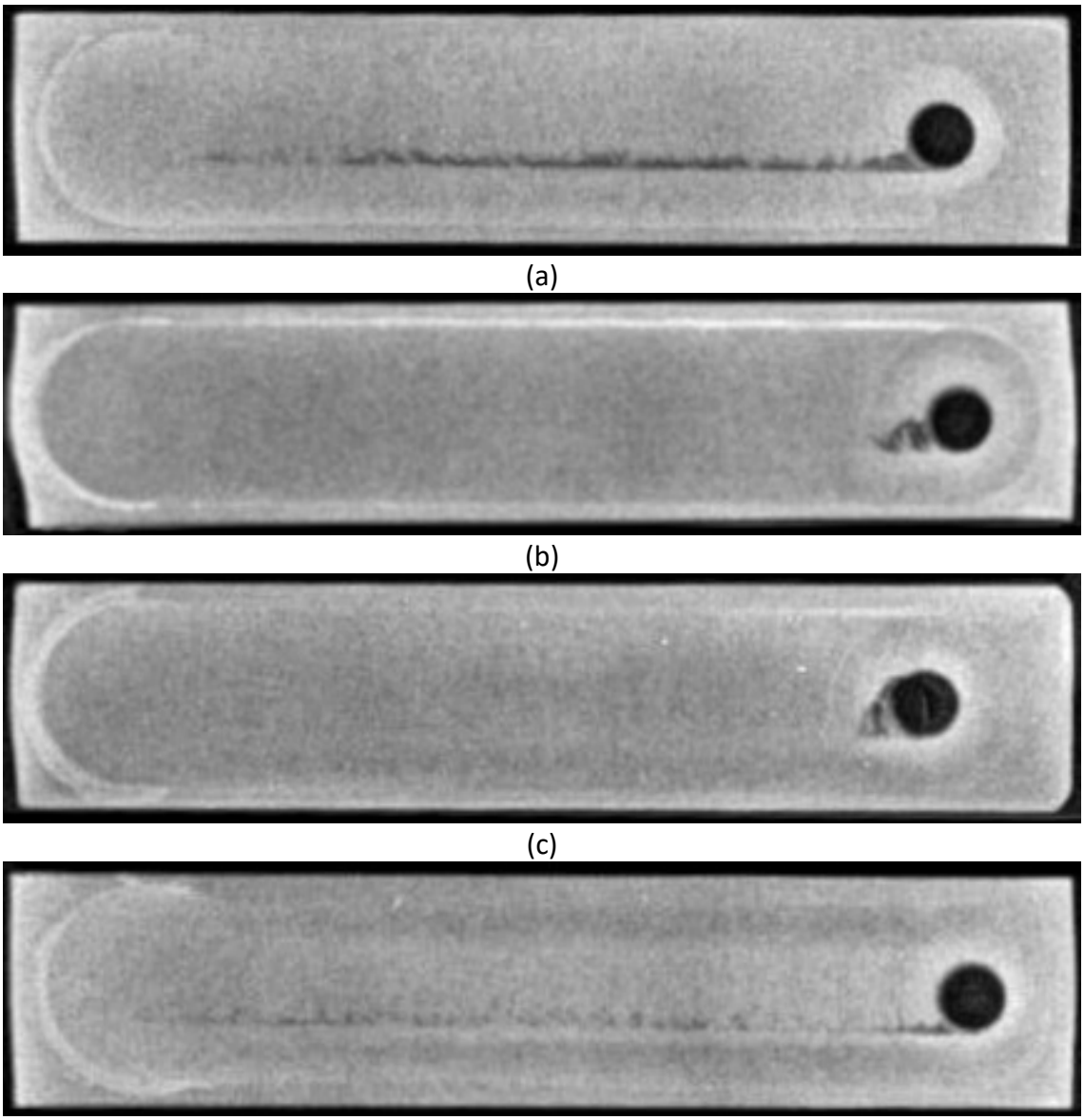

(a)

(b)

(c)

(d)

Figure 19 - X-ray radiographs of select PM2618 test specimens treated under different FSP processing conditions. (a) 63 mm min^{-1} @ 1125 RPM (fail), (b) 63 mm min^{-1} @ 710 RPM (pass), (c) 180 mm min^{-1} @ 1400 RPM (pass), (d) 180 mm min^{-1} @ 710 RPM (fail). Darkened points indicate the presence of internal voids. All specimens in the T1 temper.

Table 7 - Summary of the X-ray inspection results for PM2618 specimens after FSP.

	A - Spindle Speed (RPM)							
	710	710	710	710	900	900	900	900
B - Traverse Speed (mm/min)	63	90	125	180	63	90	125	180
A/B (mm/revolution)	0.089	0.127	0.176	0.254	0.070	0.100	0.139	0.200
Pass/Fail	**Pass**	**Pass**	*Fail*	*Fail*	**Pass**	**Pass**	*Fail*	**Pass**
	A - Spindle Speed (RPM)							
	1125	1125	1125	1125	1400	1400	1400	1400
B - Traverse Speed (mm/min)	63	90	125	180	63	90	125	180
A/B (mm/revolution)	0.056	0.080	0.111	0.160	0.045	0.064	0.089	0.129
Pass/Fail	*Fail*	**Pass**	**Pass**	**Pass**	*Fail*	**Pass**	*Fail*	**Pass**

Each radiated sample was then sectioned, polished, and subjected to a microstructural assessment. Such examinations were completed in the unetched and etched states to affirm X-ray findings and gain a better understanding of the nature of the defects (unetched) while also providing insight on the microstructure of the SZ and surrounding material (etched). Micrographs taken from exemplary specimens representative of those found to be highly defective/defect-free are shown in Figure 20. The defects consistently occurred on the advancing side (AS) of the SZ, and as shown in Figure 20 (a) and (b), typically appeared near the top face just below the surface. These micrographs combined with the X-ray results confirmed that the voids were generally in the form of a tunnel defect. This type of defect forms when material does not fully fill in behind the tool due to inadequate plastic material flow, which can be caused by a number of factors such as insufficient heat generation or an excessive tool traverse speed [67]. Tunnel defects can also occur with excessive heat input, as this can cause the material to soften excessively such that it is extruded around the tool as flash [68]. In this sense, both of these scenarios had likely contributed to the defects observed. Samples that had a combination of low tool rotation speed and a high traverse rate (an advancement per revolution rate greater

than 0.13 mm/rev.) likely experienced insufficient heat input for the traverse speed, resulting in poor material flow. Conversely, those that had a combination high tool rotation speed and a low traverse rate (an advancement per revolution rate less than 0.07 mm/rev.) likely suffered the opposite, having an excessive heat input which caused material to flow out from around the tool. It stands to reason then that defect-free samples spanning a large range of parameter combinations were found due to those combinations resulting in the necessary amount of heat generation for the particular traverse rates utilized.

Beyond the presence of the defects in select samples, the cross sections were typical of friction stirred material. In the central region of the etched samples (Figure 20 (b and d)) a well-defined SZ was apparent, which generally etched darker than the surrounding material. When comparing the microstructure of it to that of the unaffected bulk material (BM) as seen in Figure 21 (a) and (d) respectively, Figure 17this material had underwent several notable metallurgical transitions. For one, the stirring process clearly fragmented and redistributed the relatively coarse secondary phase clusters observed in the starting as-sintered material (Figure 17) so as to yield a product with enhanced microstructural homogeneity. Second, the grains in the SZ underwent dynamic recrystallization during stirring, resulting in new equiaxed grains with a relatively consistent average size of ~2μm. Finally, this region was now seemingly devoid of the residual porosity known to be sporadically present immediately after sintering. This feature had most likely collapsed due to the appreciable amount of plastic flow that transpired in a manner consistent with that observed during upset forging of sintered aluminum alloy preforms [69].

Immediately adjacent to the SZ was the thermo-mechanically affected zone (TMAZ), which as seen in Figure 21 (b) comprised α-aluminum grains that were evidently stretched and deformed. The microstructural composition of this region somewhat parallels that seen in the bulk material in that it maintained grains with and without secondary phase

present. The secondary phase clusters and porosity along the grain boundaries were also still present, although they had begun to become broken up and scattered. While not visible in the unetched cross sections of Figure 20, a heat affected zone (HAZ) existed beyond the TMAZ. The HAZ was slightly apparent in the etched cross section of Figure 20 (d) as material below the stir track and beyond the TMAZ on either side of the SZ that etched slightly lighter than the adjacent bulk material. From the micrographs in Figure 21 (c and d) it can be seen that the HAZ was nearly identical to the bulk material. The primary notable difference was that the α-aluminium grains did not etched as darkly around their perimeter as those in the bulk. Conversely, the secondary phase particles etched to the same extent. It was postulated that thermal input to the HAZ was sufficient to dissolve a portion of the intergranular phases present so as to alter the etching response of these regions.

The macroscopic Rockwell hardness of a defect-free FSP sample (90 mm min^{-1} @ 900 RPM) was then probed with indents made in three lines that ran parallel to the longitudinal axis of the test specimen. These were positioned on the AS, SZ, and retreating side (RS) of the stir track; a similar spacing and arrangement was employed when testing the sintered (i.e. unstirred) counterpart. Data were collected for each material in the T1 and T6 states. The results are presented in Figure 22. Not surprisingly, the sintered specimen exhibited a homogenous hardness that did not vary appreciably with position, regardless of the temper condition. Here, nominal values of 56 and 70 HRB were measured in the T1 and T6 states respectively.

The hardness of the sintered + FSP specimen was comparatively less homogenous. Such heterogeneity was most pronounced in the T1 FSP bar where the highest average value existed in the SZ as compared to progressively lower values in the advancing and retreating regions of the stirred track. While varied, all averaged hardnesses in the T1 sintered + FSP sample were higher than those in the sintered T1 counterpart. The greatest

increase transpired in the SZ and amounted to a 14% improvement. Gains on the AS and RS were 10% and 3% respectively. Such differences across the stir track can be explained when the macrostructure of the stir track is considered. In this sense, the SZ was found to contain material that has been severely strained and plastically deformed (Figure 20, Figure 21) directly by the pin of the tool. In contrast, the material on the AS and RS had only been directly deformed by the rotating shoulder of the tool. This equated to a reduced severity of deformation and depth of affected material, and accordingly, inferior hardness gains relative to the starting sintered material.

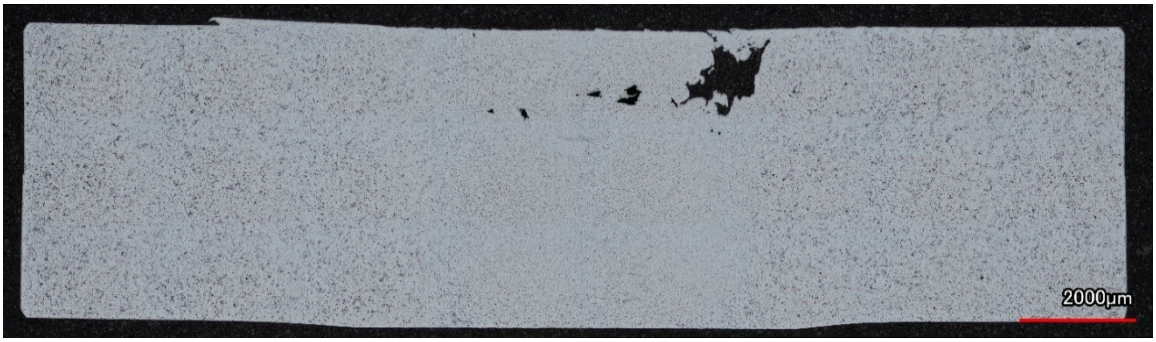

(a)

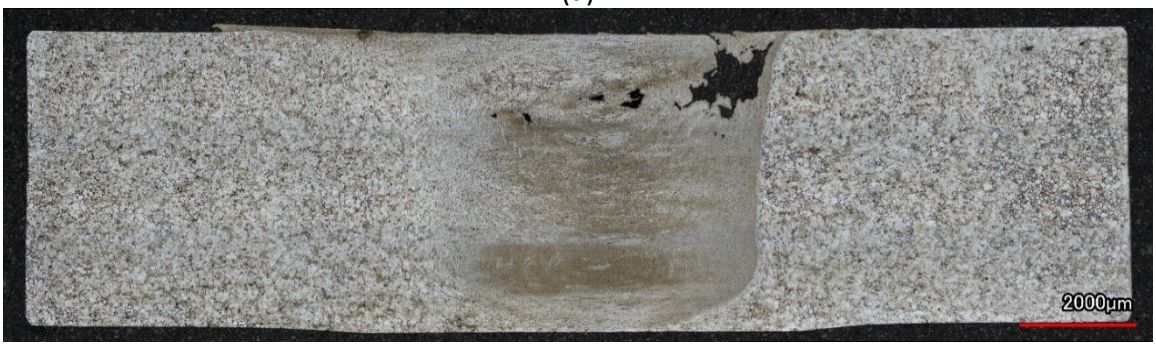

(b)

(c)

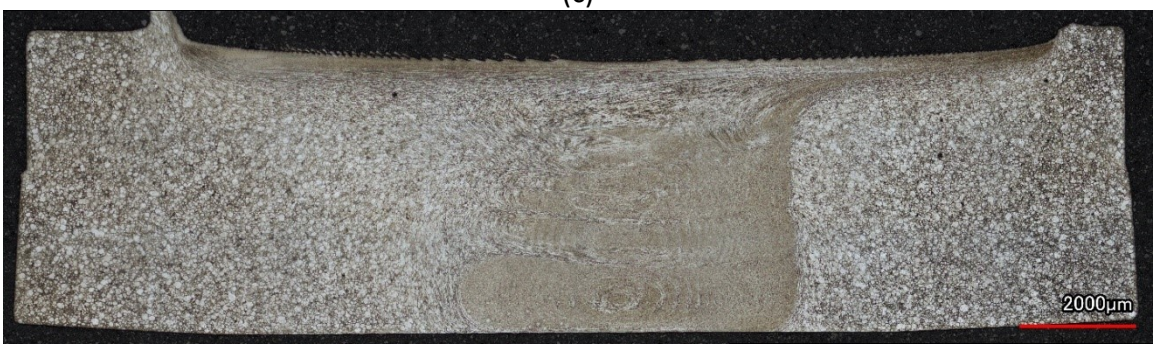

(d)

Figure 20 - Microstructures observed in PM2618 after FSP. Specimens subjected to FSP under conditions of 180 mm min^{-1} @ 710 RPM ((a) unetched, (b) etched) and 63 mm min^{-1} @ 710 RPM ((c) unetched, (d) etched). RS is on the left of all images whereas the AS is on the right. Specimens in the T1 temper.

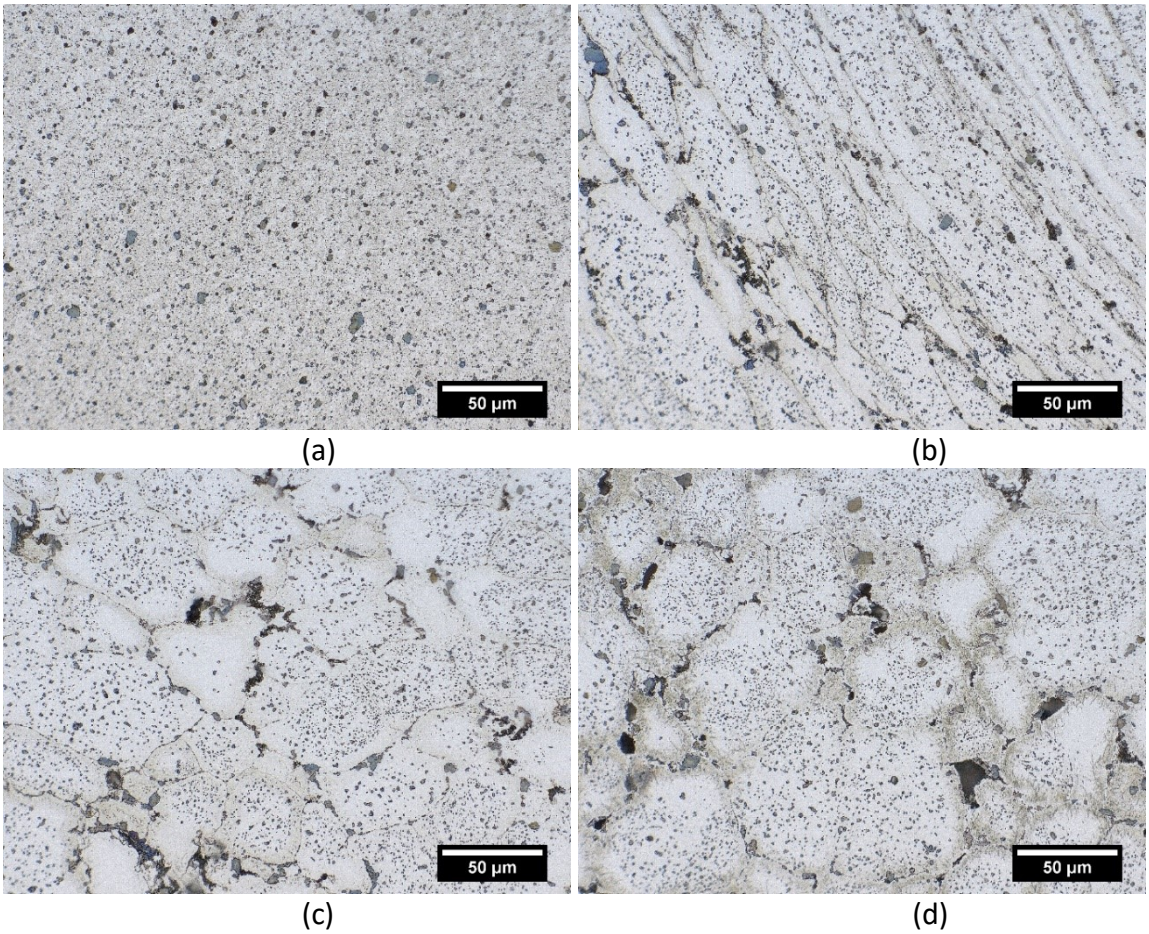

Figure 21 – Optical micrographs taken from different regions within a defect-free sinter + FSP (90 mm min^{-1} @ 1400 RPM) sample of PM2618. (a) SZ, (b) TMAZ, (c) HAZ, and (d) BM. Sample in the T1 temper.

As expected, the material that was solutionized, quenched, and artificially aged to the T6 state was appreciably harder than the T1 material. However, there was now less of a difference in hardness between the sintered material and the FSP counterpart. This was likely due to recovery occurring in the highly strained material during the initial high temperature solutionizing step of the T6 heat treatment process. FSP imparts a significant amount of strain in the material, and while some of it (i.e. that in the SZ) is able to undergo dynamic recrystallization and release its strain, the remainder is still strained to some degree. This residual strain contributes to the elevated hardness seen in the T1 sample. When heat treated to the T6 condition, the elevated temperature experienced by the

material allowed it to undergo recovery and release the residual strain. The one notable exception to this behaviour was observed on the RS which showed a 7% decrease in hardness relative to the sintered T6 product.

Of the processing parameter sets that produced defect-free samples, four that embodied the full breadth of parameters (63 mm min^{-1} @ 710 RPM, 90 mm min^{-1} @ 900 RPM, 125 mm min^{-1} @ 1120 RPM, and 180 mm min^{-1} @ 1400 RPM) were evaluated via microhardness testing. Two samples of each condition were prepared, with one retained in the T1 state while the second was subjected to T6 heat treatment. A summary of all specimens considered is provided in Table 8 while complete maps for select specimens are presented in Figure 23. In general, there were limited differences between the minimum, maximum, and average hardness across the four different processing conditions in the T1 state. The same was true for T6 samples but they did present a decisive increase in average hardness relative to their T1 counterparts that ranged from 33 to 39%.

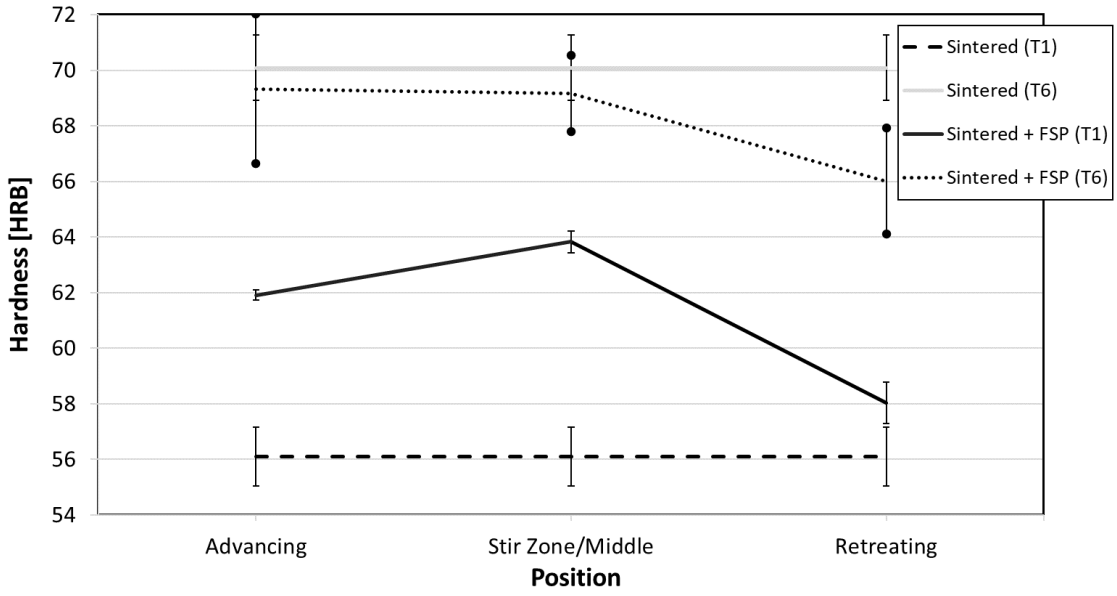

Figure 22 - Comparison of the average Rockwell hardness values measured in different regions of PM2618 test specimens (Sintered vs. Sintered + FSP) in the T1 and T6 conditions. FSP conditions of 90 mm min^{-1} @ 900 RPM were utilized.

Table 8 - Summary of the Vickers microhardness data recorded from FSP cross sections in the T1 and T6 conditions. Values deduced from the complete set of indents recorded from each cross section.

	FSP Conditions (mm min^{-1} @ RPM)			
	63 @ 710	90 @ 900	125 @ 1120	180 @ 1400
T1				
Min.	89	89	83	79
Max.	124	128	127	126
Avg.	105	109	106	105
Std. Dev.	7	8	7	8
T6				
Min.	105	102	105	108
Max.	164	159	168	165
Avg.	142	145	142	146
Std. Dev.	7	6	8	7

T1 maps (Figure 23(a)/(c)) largely paralleled the Rockwell hardness results, in that the central SZ maintained an increased hardness relative the adjacent material. The microhardness of the SZ was also relatively uniform, in keeping with the highly homogenized microstructure present (Figure 21 (a)). Cross sections of the T6 samples were noticeably different and showed somewhat of the opposite hardness trend. In this sense, the SZ remained distinguishable due to its different hardness, but now hardness was marginally lower than that in the adjacent material. Also unlike in the T1 samples, the hardness in the regions on either side of the SZ showed an apparently greater variability in hardness. This reduced uniformity of the hardness seen in the unstirred T6 material compared to what was seen in the T1 material may be due to the increased range of hardness values providing increased contrast (i.e. the difference between the minimum and maximum values in Table 8), without an actual meaningful microstructural difference.

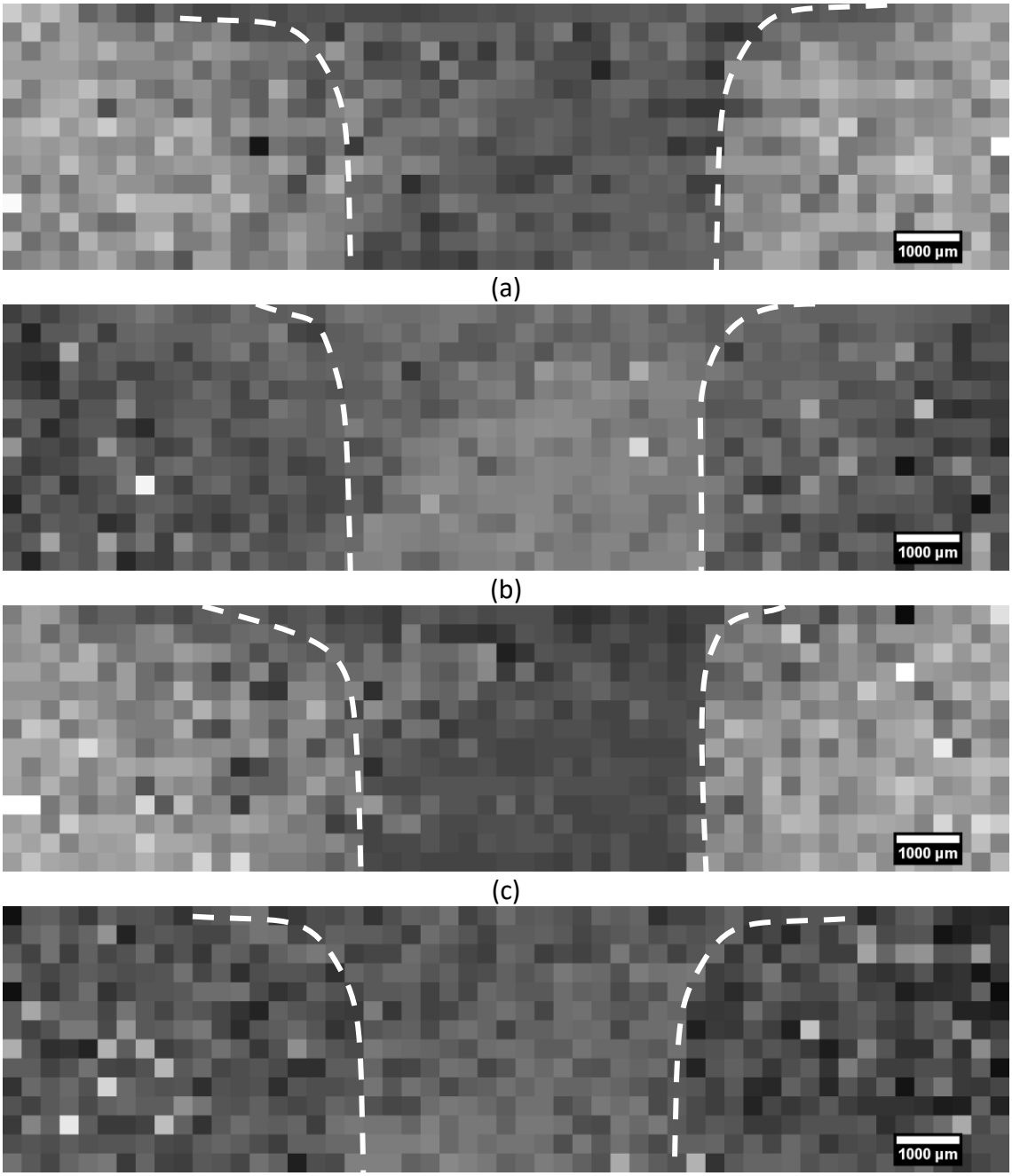

Figure 23 - Microhardness maps for FSP specimens. 63 mm min^{-1} @ 710 RPM ((a) T1, (b) T6) and 180 mm min^{-1} @ 1400 RPM ((c) T1, (d) T6). Dashed lines indicate the approximate boundary of the SZ. RS is on the left whereas the AS is on the right in all images.

XRD of FSP materials was then conducted to assess if changes to the nominal phase composition had occurred as a result of stirring. An exemplary trace recorded from a FSP specimen is shown in Figure 24. This was nearly identical to the sintered material trace in

Figure 18, indicating that FSP had negligible affect on the phase composition. The same secondary minor peaks were observed in both samples. The intense frictional heating induced during FSP can be upwards of 80% of the absolute melting temperature of the alloy [70], [71], and could reasonably be expected to have a noticeable effect on the phase composition of the material, however no substantial differences were observed. In addition to the S- and θ-type precipitates (Al_2CuMg and Al_2Cu, respectively), PM2618 gains some degree of strength from several secondary phases which contain iron and nickel. These phases impart a significant degree of thermal stability since they do not readily diffuse into the bulk material at high temperatures, and as such appear to have been relatively unaffected by stirring. Conversely, the S- and θ-type precipitates are not nearly as thermally stable and would be expected to partially re-enter solid solution in the SZ. The temperature rapidly decreases immediately outside of the SZ, and the precipitates in those regions would age and grow instead of dissolving. Since PM2618 naturally ages to some extent at room temperature it would be expected that precipitation would later re-occur in the SZ, and as such result in the relevant peaks on the diffraction pattern appearing.

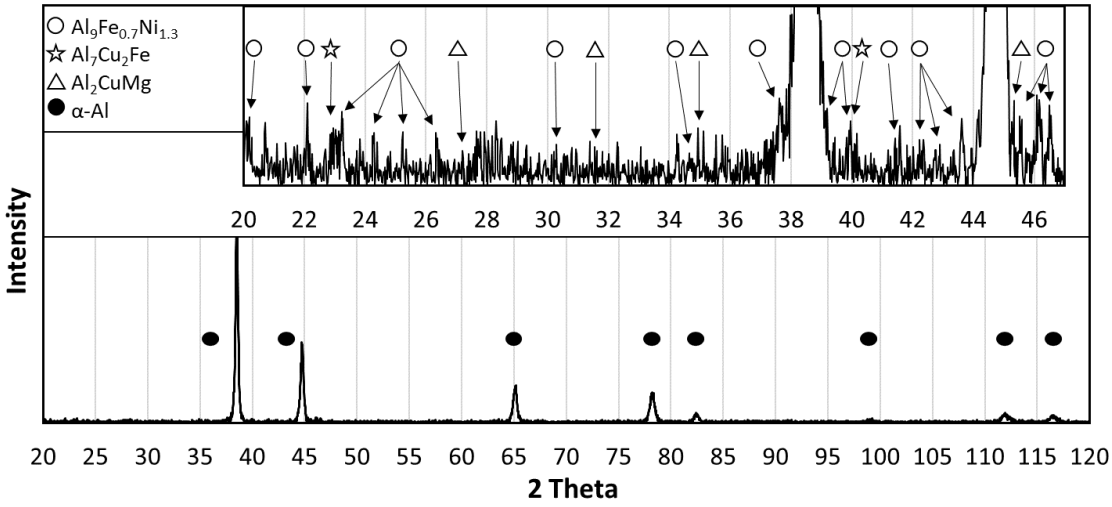

Figure 24 - XRD pattern recorded from a PM2618-T1 test specimen after FSP (90 mm min^{-1} @ 900 RPM). Inset trace is a magnified view that enhances the secondary peaks observed.

5.4.3 Friction Stir Welded (FSW) Specimens

To determine the applicability of processing conditions deemed successful in FSP, several (Table 5) were then utilized to FSW pairs of PM2618 bars. Characterization commenced with microstructural assessment. Optical micrographs of the etched microstructure for each welding condition are shown in Figure 25. In each instance the original boundary between the pair was no longer discernable. As such, their general appearance was found to be practically identical to FSP counterparts (Figure 20 (d)). Close examination with optical microscopy revealed that, like the FSP samples, these too were free from tunnel defects and voids. Additionally, none of the defects that can occur in FSW were observed, such as root flaws and s-curve defects. Root flaws occur when the weld does not penetrate the full thickness of the joint, leaving a tight crack-like defect in the weld root that significantly deteriorates mechanical properties [72]. S-curves or zigzag lines are the result of the alumina layer from the contacting surfaces not being adequately broken up and dispersed during stirring. When heat treated this type of defect can form microcracks and seriously deteriorate mechanical properties [73]. The lack of these FSW-specific defects indicated that the stirring action invoked by the selected processing parameters was sufficiently vigorous to form a high-quality joint.

Figure 25 - Etched microstructures observed in PM2618 after FSW. Specimens subjected to FSW under conditions of (a) 63 mm min^{-1} @ 710 RPM, (b) 90 mm min^{-1} @ 900 RPM, (c) 125 mm min^{-1} @ 1120 RPM, and (d) 180 mm min^{-1} @ 1400 RPM. RS is on the left of all images whereas the AS is on the right. Specimens in the T1 temper.

SEM was then utilized to examine the microstructure of the BM and the SZ that was manifested under each set of processing parameters. Not surprisingly, electron micrographs of the BM (Figure 26 (a)) were consistent with optical micrographs of the starting material (Figure 17). In this sense, the bulk of the α-aluminum grains contained a fine dispersion of small secondary phase particles, while a small fraction was completely devoid of these particles. Relatively large clusters of secondary phase material were also noted as was a small fraction of porosity; the latter was visually distinct due to the bright charging effect on the edge of the pores. Micrographs of the SZs (Figure 26 (b) - (e)) were also very much comparable to themselves and the FSP material. Most notably, the SZ microstructures were highly homogenized, with the secondary phase clusters having been broken up and dispersed evenly throughout the material. All four processing conditions resulted in very similar levels of disruption and dispersion of the secondary phase material as well as an effective elimination of porosity. One possible reason for this similar behaviour is that all four processing parameter pairs had similar rates of tool advancement per revolution (ranging from 0.09 to 0.13 mm/rev), resulting in a comparable volume of material being displaced and stirred per revolution as the tool advanced.

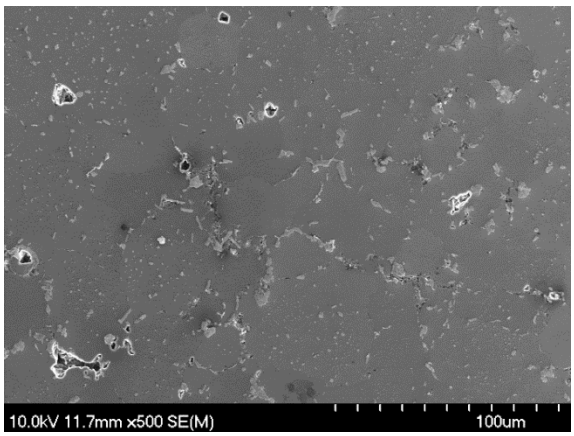

(a)

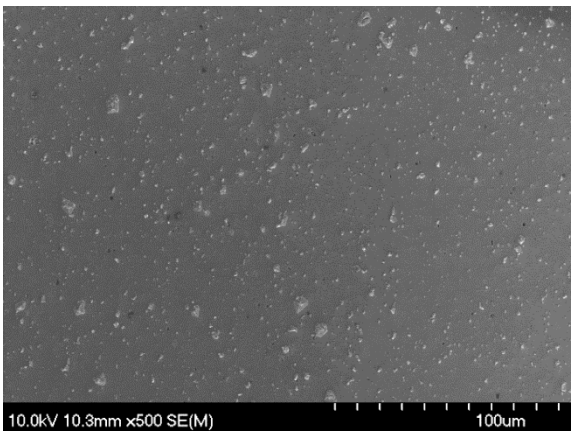

(b)

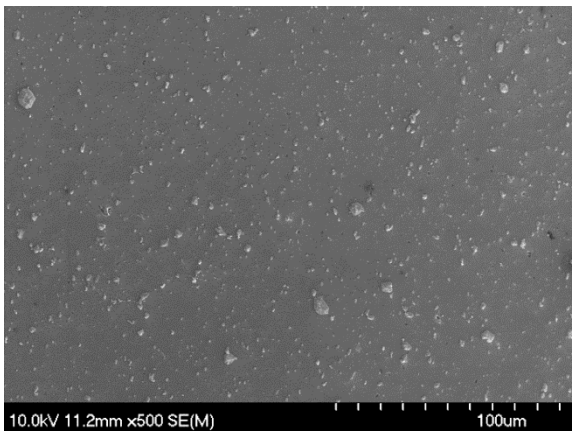

(c)

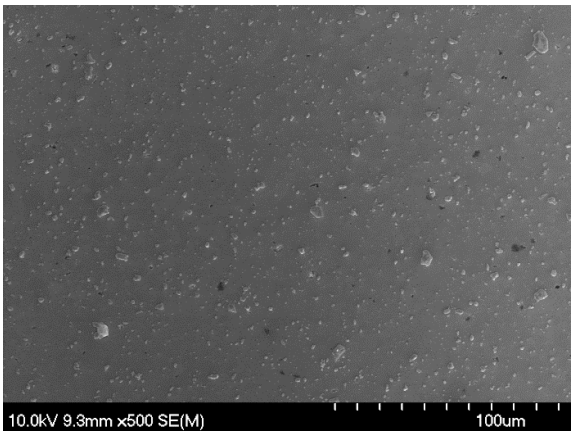

(d)

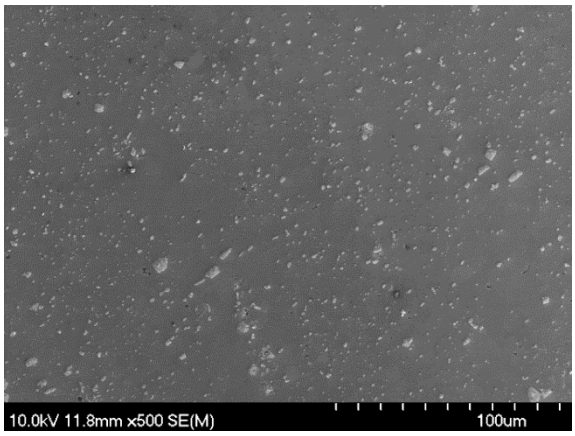

(e)

Figure 26 – SEM images of the microstructures observed in PM2618. (a) BM and (b) the SZ region of a sample subjected to FSW at 63 mm min^{-1} @ 710 RPM, as well as SZ regions of samples stirred at (c) 90 mm min^{-1} @ 900 RPM, (d) 125 mm min^{-1} @ 1120 RPM, and (e) 180 mm min^{-1} @ 1400 RPM.

To investigate the effect of the different processing parameters on the mechanical properties of welds, three-point bend testing was conducted as a simple static load to fracture and as a dynamic fatigue loading. In all cases, samples were oriented such that the maximum stress was positioned on the middle of the stir weld, with the top surface loaded in compression and the root in tension. A representative pair of stress-displacement curves are given in Figure 27 that illustrate key findings. The include the facts that FSW had imparted a significant improvement in overall performance and the respective properties (in bending) of Young's modulus, yield strength, UBS, and total displacement to fracture. This was ultimately found to be consistent in all FSW specimen as shown in Figure 28 where a complete summary of the data is presented. Figure 28(a) shows that minor increases in Young's modulus were observed, ranging from 9% to 23% relative to the as sintered material. More notable were the sizable gains in yield strength, UBS, and total displacement to fracture within the FSW specimen (Figure 28(b) and (c)). Yield strength (0.2% offset) demonstrated a nominal increase of 33% as average values for the welded samples ranged from 464 to 474 MPa as compared to only 352 MPa for the as-sintered counterpart. Likewise the UBS improved by ~35%, increasing from 600 MPa as-sintered to ~800 MPa after FSW. One of the most drastic changes seen in the FSW samples, as demonstrated in Figure 27 and Figure 28 (c), was the significant increase in ductility as averge values were generally more than double that of the sintered material.

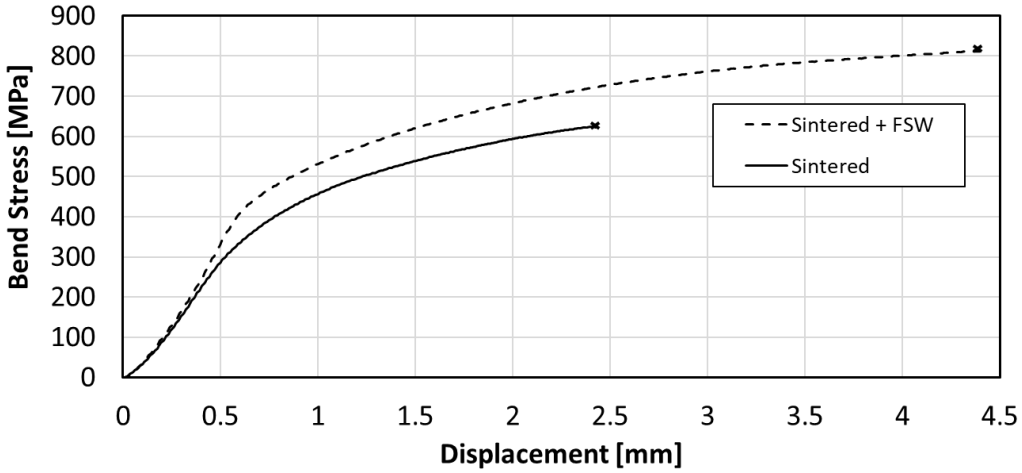

Figure 27 – Representative bending stress vs displacement curves for samples in the as-sintered and sintered + FSW (90 mm min^{-1} @ 900 RPM) conditions.

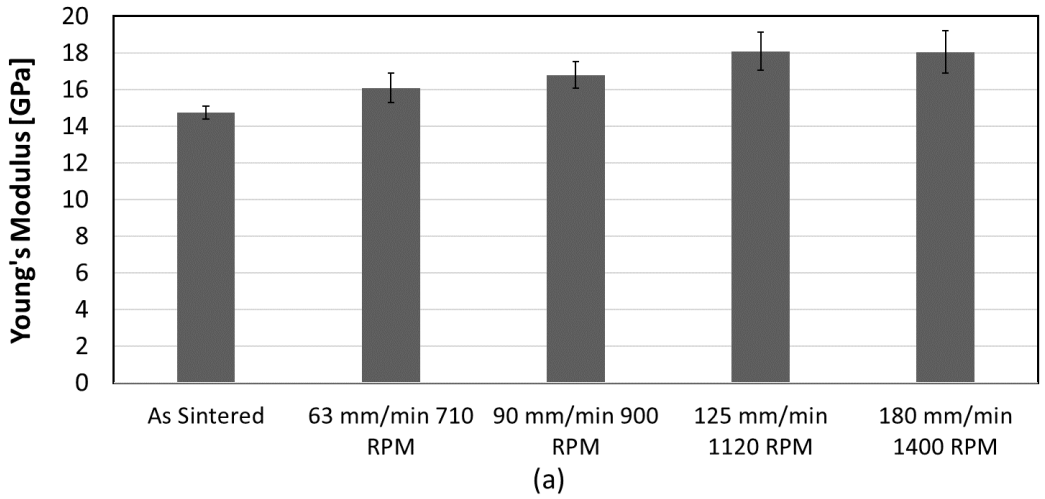

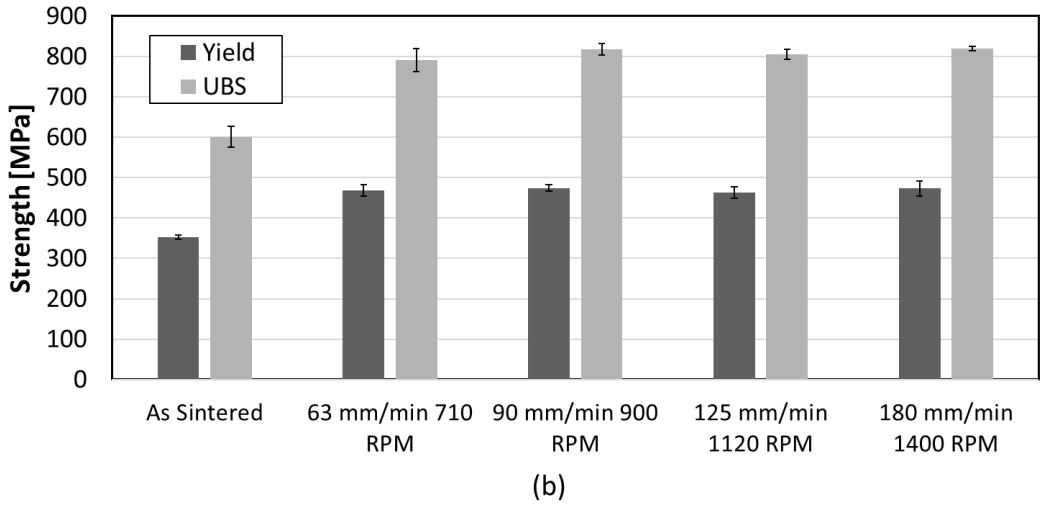

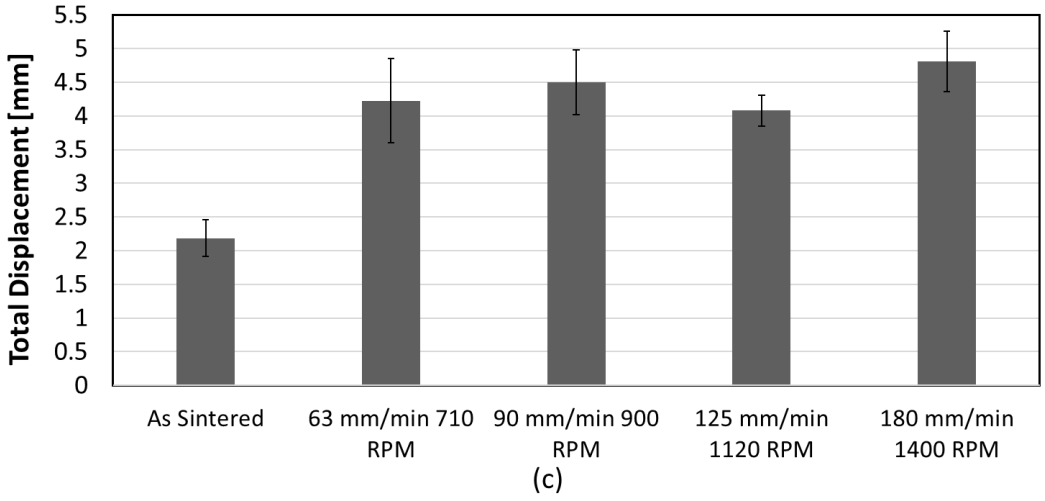

Figure 28 – Static bend testing results for FSW products. (a) Young's modulus, (b) yield strength/UBS, and (c) total displacement to fracture.

To characterize the fatigue behaviour of the FSW joint, cyclic loading was performed in a three-point bending configuration. Between 15 and 18 samples were tested for each processing parameter as well as the base material. The results presented in Table 9 give the fatigue strength for which it is estimated that N% of samples would pass 10^6 cycles at a load of "σ_N". When considering the σ_{50} strengths, the FSW material all showed a decisive improvement over the sintered material, with an increase ranging from 22% to 32%. While the improvement in σ_{50} was fairly consistent, the changes to the σ_{90} and σ_{10} values can not be overlooked. Two conditions (63 mm min^{-1} @ 710 RPM and 180 mm min^{-1} @ 1400 RPM) had a relatively narrow range between their σ_{90} and σ_{10} strengths (±10 and 12 MPa, respectively) while the others (90 mm min^{-1} @ 900 RPM and 125 mm min^{-1} @ 1120 RPM) had comparatively large ranges (±107 and 80 MPa, respectively). A narrow range is the desired result, as it would imply that the associated FSW processing parameters had resulted in a consistent and repeatable alteration to the material. Conversely, a large spread in the data suggests that the choice of parameters offers inconsistent results.

Table 9 - Bending fatigue strength data for sintered and FSW samples of PM2618.

Processing Conditions	**Fatigue Strength [MPa]**		
	σ_{90}	σ_{50}	σ_{10}
Sintered	221	235	249
Sintered + FSW (63 mm min^{-1} @ 710 RPM)	283	293	303
Sintered + FSW (90 mm min^{-1} @ 900 RPM)	184	291	397
Sintered + FSW (125 mm min^{-1} @ 1120 RPM)	231	310	390
Sintered + FSW (180 mm min^{-1} @ 1400 RPM)	274	286	298

While the varied ranges between the σ_{10} and σ_{90} values may be inherent to the specific parameters chosen, this dichotomy in behaviour between the different parameter sets could also be an artifact of the staircase testing method itself. In this sense, if several specimen fail in succession followed by several passing in succession the data takes on a larger spread than if the specimen alternate more frequently, even for the same overall number of passing and failing specimen. The possibility that the increased spread in the data is a result of the specific specimen used and the order they were tested in and not the processing conditions is further reinforced by the fact that the mechanical property data presented in Figure 28 has a relatively consistent range across all four processing parameter sets.

The noted gains in mechanical properties as a result of FSW can largely be attributed to microstructural changes. For one, the significant reduction in grain size in the SZ brings about the most well known of strengthening mechanisms; grain-boundary (or Hall-Petch) strengthening. In this case the reduction in average grain size results in more grain boundaries present per unit volume, which in turn present an increased impediment to dislocation motion and an increase in the strength of the material. The TMAZ itself presents an additional strengthening mechanism, as the material has not undergone recrystalization like that of the SZ and hence retains strain and the concomitant increased dislocation density induced by deformation, thus becoming locally hardened. Further strengthening comes from the disruption and redistribution of the secondary phase material, which has been spread throughout the SZ in a significantly more homogenous distribution. The reduction of the residual porosity would provide yet another a strengthening benefit as such features can serve as crack initiation sites and even small fractions of residual pores can have a decisively negative impact. Finally, similar 2xxx APM alloys are known to maintain a nominally continuous network of nano-metric scale oxides such as Al_2O_3, MgO, and $MgAl_2O_4$ after sintering. It is known that thermo-mechanical work can disrupt the network and gives rise to appreciable gains in static and dynamic mechanical properties [69],[74]. As such, it is highly plausible that FSW has invoked similar

changes to the nano-oxide network in PM2618 and that this has also contributed to the mechanical gains realized.

Even though fatigue specimen were consistently loaded with the greatest stress located on the center of the weld line (i.e. directly on the middle of the SZ), fracture was not always guaranteed to occur there. Ultimately, it was found to transpire in one of three distinct zones: (i) on the RS through the TMAZ/HAZ, (ii) on the AS through the TMAZ/HAZ, or (iii) through the SZ itself. For three of the four FSW parameter combinations there was no apparent trend of fracture preferentially occurring in one region more so than the others. The notable exception was when welding under conditions of 63 mm min^{-1} @ 710 RPM as these specimens fractured exclusively through the SZ. When fracture occurred in the SZ the fracture plane was oriented vertically, and the surface (on a macro scale) was flat and parallel to the pin that applied the load. However, when the fracture occurred on either the RS or AS of the SZ the fracture was no longer planar and exhibited a degree of curvature. Additionally, when fracture occurred outside of the SZ the plane of the fracture tended to have a slight tilt relative to the SZ; towards the SZ at the top and away at the bottom.

Exemplary fracture surfaces that correlated to each fracture zone location were then examined through electron microscopy in addition to one from a specimen tested in the as-sintered T1 state. In all cases, fracture consistently originated the bottom surface coincident with maximum tensile stress and none of the failures showed evidence of any macroscopic sub-surface defects such as those discovered during X-ray inspection (Figure 19). For fractures that occurred on the RS and AS (Figure 29 (a) and (b)) the area immediately around the fracture origin appeared very similar, with the surface taking on a wavy, twisted appearance radiating outwards from the origin. One reason for this similarity in appearance to each other, but not other failure locations, is that both AS and RS fractures are in the TMAZ material to either side of the SZ, which should have

experienced similar thermo-mechanical effects from stirring. Interestingly, fracture on the AS had more porosity visible than the RS failure. One possible reason for this difference is that the thermo-mechanical action from stirring had a greater deformation affect (and hence acuity of pore collapse) on the RS side. For fractures that originated in the SZ (Figure 29(c)), the surface had a similar appearance to the RS/AS fractures, but on a significantly finer scale. This difference was likely due to the very fine microstructure in the SZ. Another visibly notable feature was the consistently spaced vertical wavy pattern. This feature appeared to be independent of the actual fatigue fracture striations and was possibly related to how the material flowed around the tool during FSW. The fracture origin in the bulk material showed the most obvious presence of porosity in addition to secondary cracks, some of which connected multiple pores. This highlighted the critical role that residual porosity played in dictating overall fatigue behaviour.

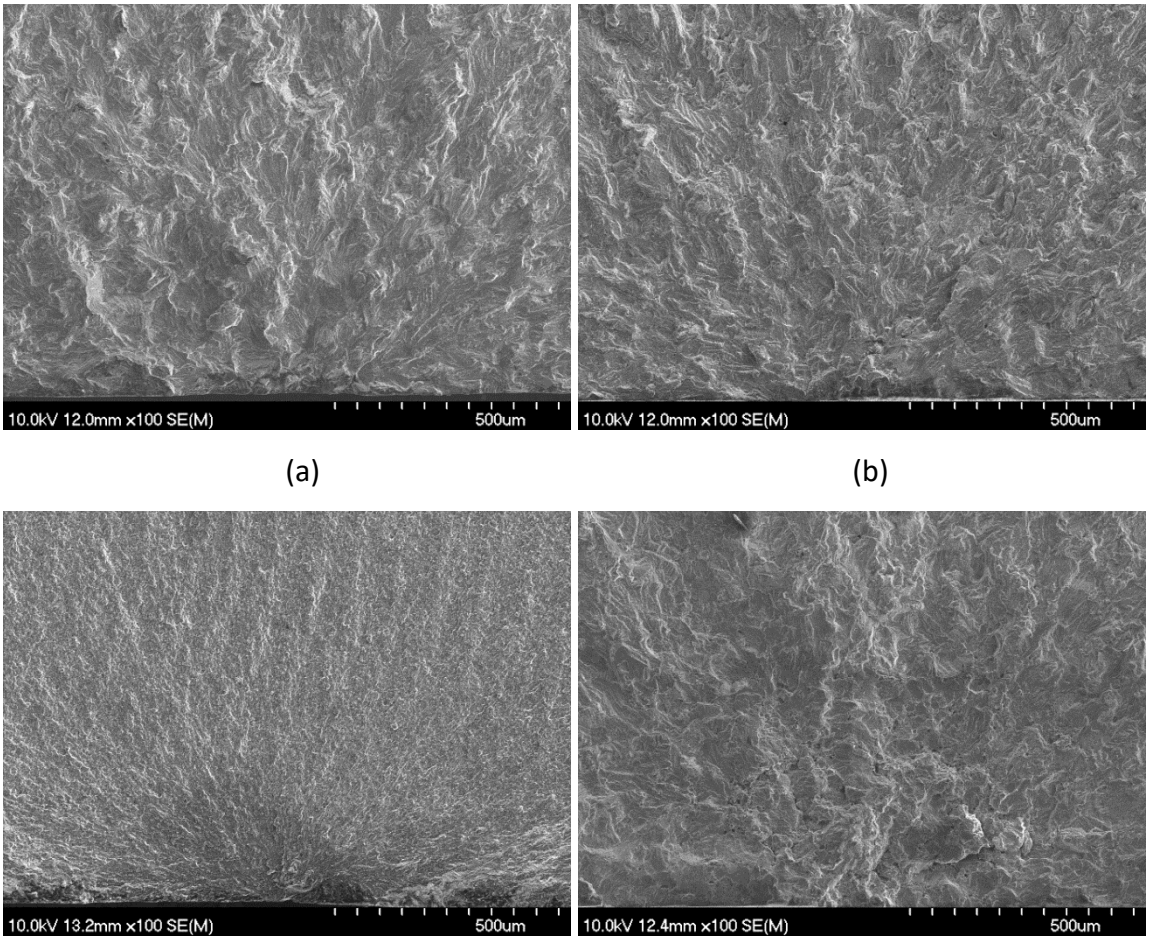

Figure 29 - Images of the locations where fatigue cracks had originated in FSW products that failed in the (a) RS, (b) AS, and (c) SZ. Fracture origin in an as-sintered specimen is shown in (d).

Once a fatigue crack has originated, it will then generally advance in a steady-state manner for an extended number of cycles. Steady-state fracture is visually distinct from other regions as it is caused by the slow progression of the crack with an incremental advancement during each load cycle that frequently leads to a stepped appearance. Steady-state fractures through the RS and AS regions (Figure 30(a) and (b)) again had a similar appearance to each other. In both cases straight to slightly curved striations typical of the cyclic loading were clearly visible. Cracks had primarily advanced in a transgranular manner although there was minor evidence of intergranular failure in the fracture on the

AS. The same period of fracture in a SZ failure (Figure 30(c)) was also highly transgranular but now it was much finer in size commensurate with the refined grain size of this region. In all three cases, the steady-state fracture zone was relatively flat. Steady-state fracture in the as-sintered material (Figure 30(d)) was notably different from the FSW materials. Here, the fracture surface maintained appreciably variations in topography. Some evidence of transgranular fracture prevailed but the dominant mode was intergranular. Such differences were ascribed to the break-up of the residual oxide networks in the FSW systems and the lack thereof in the as-sintered counterpart.

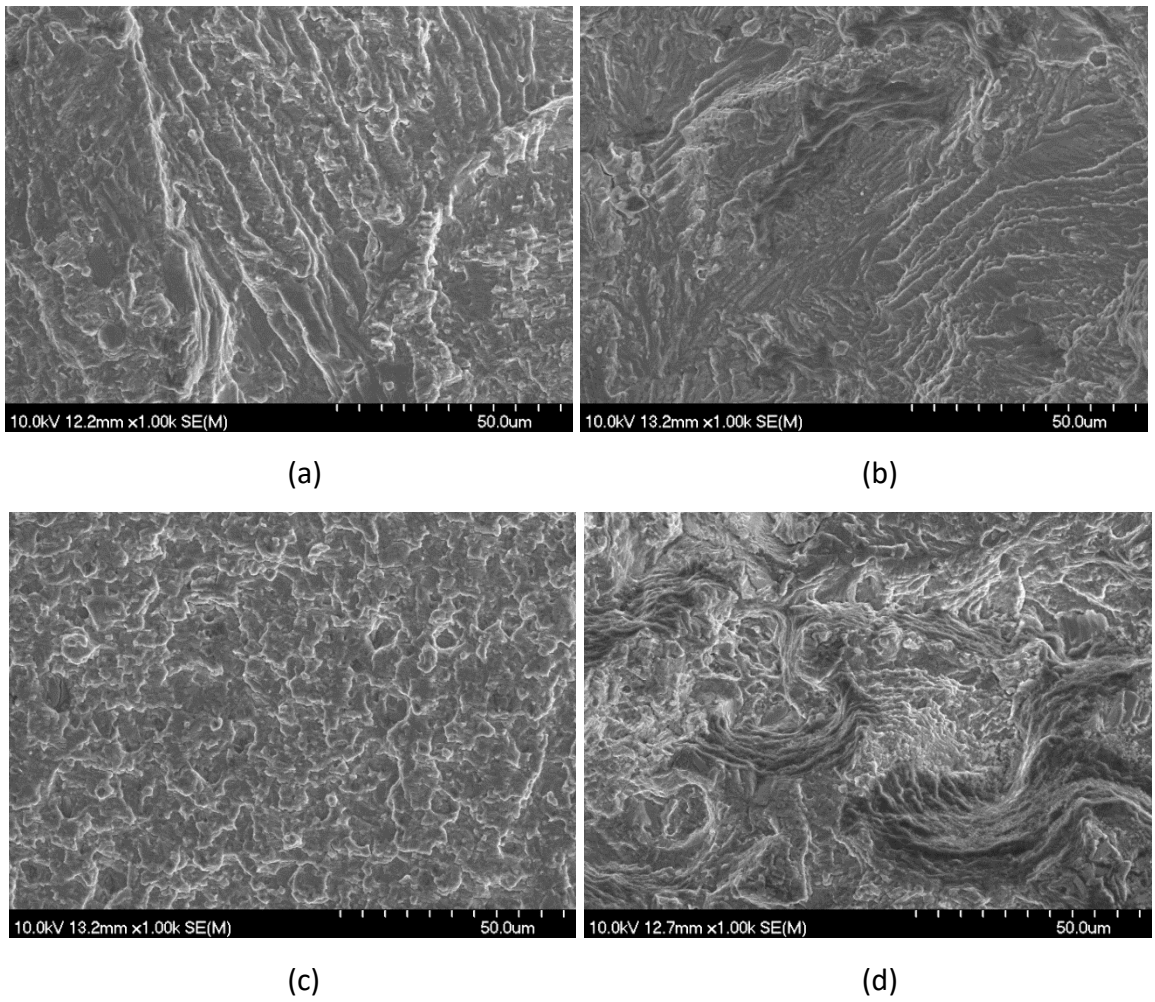

Figure 30 - Images of the steady-state fracture region in FSW products that failed in the (a) RS, (b) AS, and (c) SZ. Steady-state fracture in an as-sintered specimen is shown in (d).

5.5 Conclusions

In the course of investigating the application of FSP and FSW to the APM alloy PM2618, the following conclusions were reached:

1. X-ray radiography and microstructural analyses confirmed that PM2618 could be successfully processed via FSP and FSW under a variety of process parameter combinations.
2. FSP and FSW resulted in significant microstructural improvements within the SZ. This was manifested as a reduced grain size, enhanced homogeneity in terms of secondary phase size/distribution, and the elimination of residual porosity. Such changes did not invoke discernable alterations to the nominal phase composition.
3. Hardness of T1 samples increased as a result of FSP/FSW but the gains were found to vary through the stirred cross sections. A T6 heat treatment improved the hardness further but now sintered and FSP/FSW materials became comparable in this regard.
4. Three-point bend testing confirmed that T1 FSW products exhibited improved static bend strength properties as well as bending fatigue behaviour relative to the as-sintered material.

Acknowledgements

The Author would like to acknowledge the Natural Sciences and Engineering Research Council of Canada (NSERC) for financial support via Discovery Grant 250034-2013. Laboratory assistance provided by colleagues at Dalhousie University (Randy Cooke, Patricia Scallion, Angus MacPherson, Mark MacDonald, and Albert Murphy) and at the University of Waterloo (Luqman Shah) is gratefully appreciated as well.

Chapter 6.0 Friction Stir Processing of Aluminium Powder Metallurgy Alloy TC2000

In a secondary stream of FSP research, tests were completed on the commercial APM alloy known as TC-2000 (Al-1Mg-1.5Sn). Test specimens of this material were fabricated in accordance with the same procedures followed with PM2618, the only exception being the use of a slightly higher sintering temperature (630°C). The microstructure of the sintered material (Figure 31 (a)) was mainly composed of grains of the primary α-aluminium phase. Intermetallic Mg_2Sn formed during sintering and was found to be present at the grain boundary regions, faintly appearing as a slightly darker shade of grey, partially outlining the bulk aluminium grains. Also visible in between the grains as very dark, often black spots were isolated pockets of the residual porosity.

FSP was performed on TC-2000 with different spindle speeds (710, 900, 1120, and 1400 RPM) and traverse speeds (63, 90, 125, and 180 mm/min), resulting in 16 unique processing parameter combinations. The material of the stir zone (Figure 31 (b)) was markedly different from that in the as-sintered condition, with no semblance of the previous structure of the Mg_2Sn and residual porosity. The stirred material presented a highly refined microstructure, appearing to primarily consist of a fine dispersion of Mg_2Sn and very small pores in a bulk α-aluminium matrix. Scattered among this fine dispersion were the occasional larger pore and slightly larger Mg_2Sn fragment which survived being broken up by the intense stirring action.

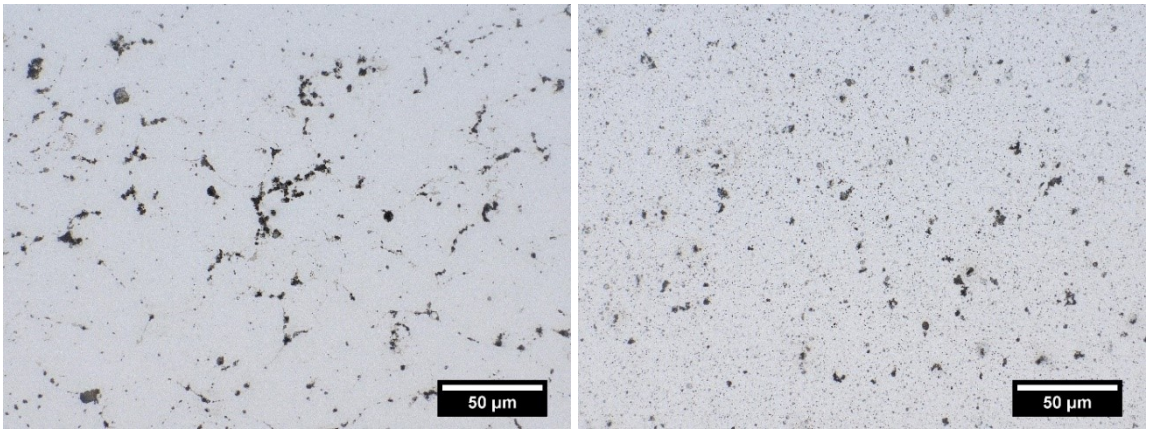

(a) (b)

Figure 31 - Microstructures of TC2000 as observed through optical microscopy. (a) As-sintered and (b) within the stir zone after FSP (90 mm min^{-1} @ 900 RPM).

X-ray diffraction was performed to investigate whether the stirring had any effect on the phase composition. The diffraction pattern for TC2000 contained two sets of peaks, as shown in Figure 32, with the main large peaks corresponding to the primary α-aluminium phase, while several smaller low angle peaks were found to belong to the Mg_2Sn phase. Both the sintered and FSP samples had near identical diffraction patterns, indicating that FSP had no noticeable effect on the phase composition. Even though the increased temperatures experienced during FSP can be as high as 80% of the alloys absolute melting temperature [67], the lack of change in phase composition is to be expected owing to the thermal stability and relatively high melting temperature of Mg_2Sn (773°C [75]) being above that of the bulk aluminium, overall preventing it from dissolving back in to the aluminium during stirring.

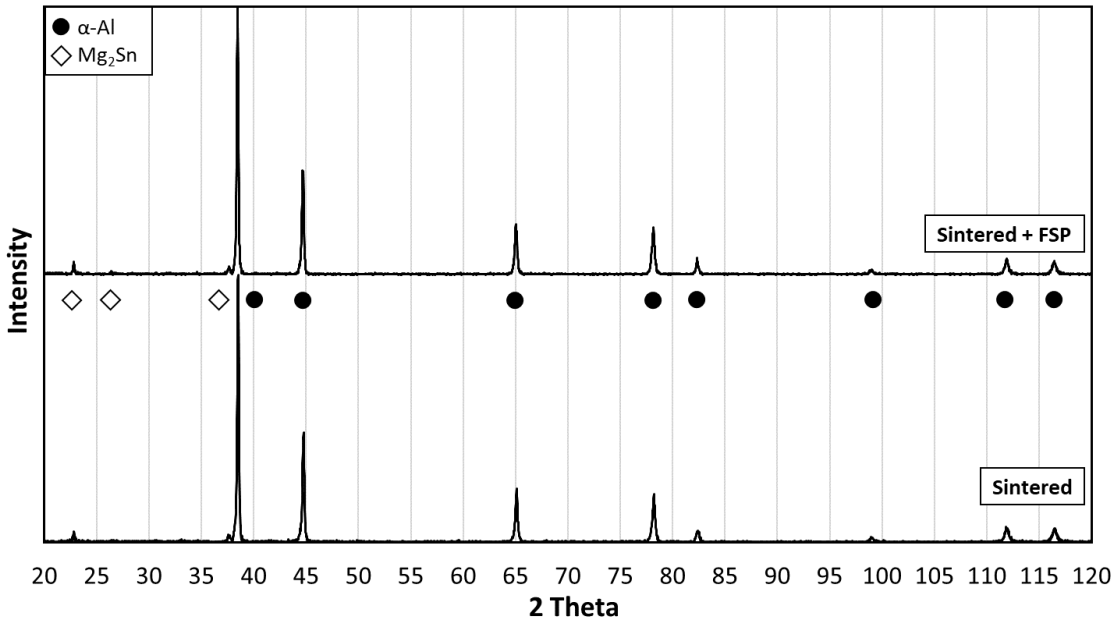

Figure 32 - X-ray diffraction patterns recorded from TC2000 samples in the sintered as well as the FSP (90 mm min^{-1} @ 900 RPM) condition.

The effects of FSP on the thermal properties of the alloy was investigated by subjecting FSP material and as-sintered material to laser flash analysis (LFA). Material for the FSP specimen was taken directly from the center of the stir zone and testing was conducted at room temperature (21°C). Simply put, LFA is used to determine the thermal diffusivity of a material by heating one side of a sample and measuring the temperature rise on the opposite side over time. The thermal conductivity can be calculated by multiplying together the heat capacity of the material (previously determined by Smith *et al.* [23]), the density of the material, and its thermal diffusivity. As shown in Figure 33, FSP imparted negligible change in the thermal conductivity of the material. Two factors which have a significant effect on the thermal properties are the composition of a material and (especially pertinent for APM alloys) the degree of porosity [22]. As seen in the XRD results in Figure 32 FSP did not affect the phase composition of the alloy, and from the micrographs in Figure 31 the material was already seen to be highly dense (average sintered density was found to be 99.8% of theoretical maximum) which only stood to be

further improved by the FSP process. It should come as no surprise then that FSP had no meaningful effect as these two critical properties were unchanged by FSP.

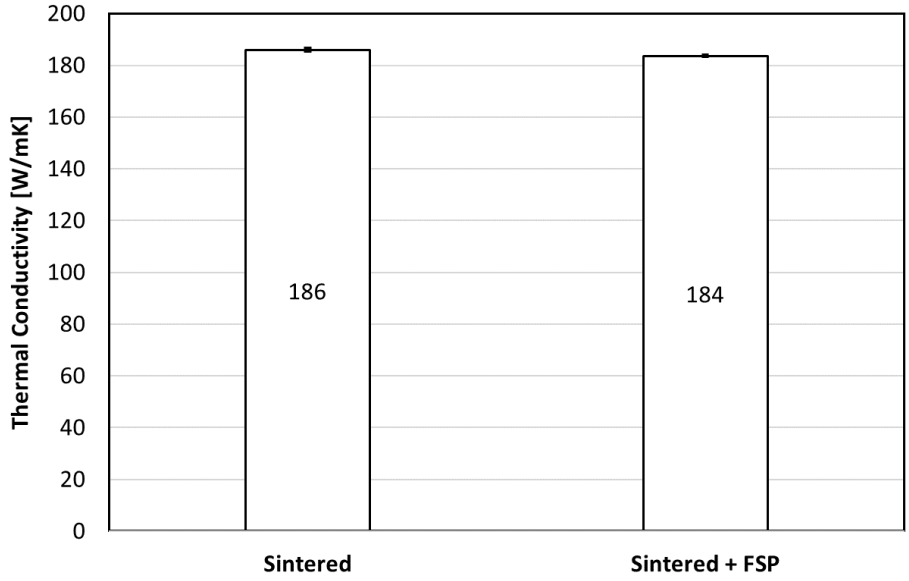

Figure 33 - Thermal conductivity of TC2000 in the as-sintered and the post-FSP (90 mm min^{-1} @ 900 RPM) condition.

FSP specimen were then subjected to X-ray radiographic examination to investigate the presence of internal voids and flaws. Visually, the majority of samples exhibited a smooth, clean surface and showed no outward indications of defects. However, when examined radiographically it was found that all of the specimens had some form of internal defect along the stir track. Due to the nature of the radiographic technique areas of low density (i.e. voids) appear darker than the surrounding material. Accordingly the defects seen in the samples (Figure 34) appear as dark lines, which are discontinuous in some samples, along the advancing side of the stir track. In some specimen the defect spanned the entire length of the stir track, while in others the defects only appearred at the start and end of the track. The longitudinal nature of the defects seen in the X-rays is highly indicative of a tunnel defect, which is a type of defect that forms as a result of material not fully backfilling behind the tool due to inadequate plastic material flow. Since all specimen

contained defects it was difficult to determine if the primary cause was underheating or excessive tool traverse speed. Underheating may be a more credible cause, however, as the relatively high thermal conductivity of the alloy may have resulted in insufficient heat being generated at the stir zone due rapid dissipation.

In addition to the defects seen in the stir zone, 10 of the 16 specimen also exhibited cracks on the retreating side where the tool initially plunged into the material. Nominally, during the initial plunge of the tool into the workpiece sufficient heat is generated to allow the material to soften to the extent that it flows up and around the tool as flash. The cracks extending radially away from the insertion point would seem to indicate that the plunge rate used was too high for the amount of heat being generated, causing the material to be pushed away from the tool instead of flowing around it.

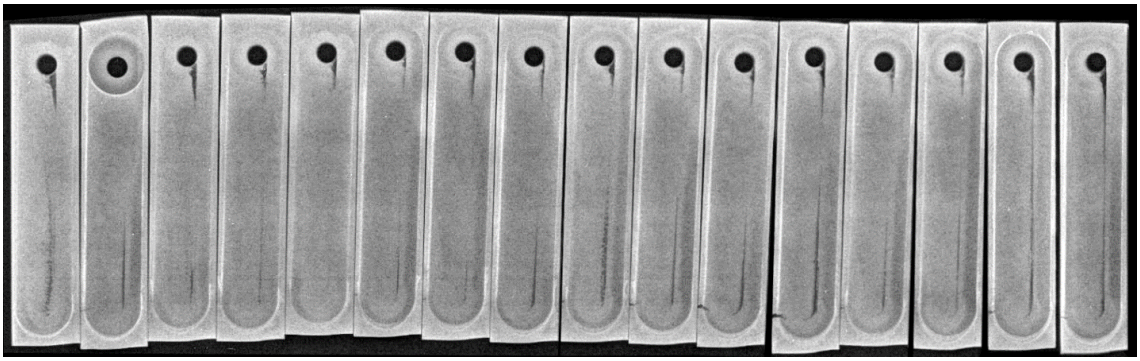

Figure 34 - X-ray radiograph of TC2000 test specimens treated under different FSP processing conditions.

Hardness measurements of the surface of a sintered specimen and on the stir track of an FSP specimen (90 mm min^{-1} @ 900 RPM) was taken using a Rockwell hardness tester. Indents were made in three parallel lines along the length of the stir track of the FSP sample, positioned on the AS, SZ, and RS of the stir track; with a matching spacing and arrangement used when testing the sintered (i.e. unstirred) sample. The bulk material was found to have an average hardness value of 49 HRH, with a relatively wide standard deviation of 4 HRH. The overall hardness of the stir track of the FSP specimen was found

to be elevated compared to the bulk material. Per Figure 35, the hardness varied with position across the width of the stir track, with the material in the middle (i.e. directly over the SZ) displaying the greatest increase (44%). The material on the advancing and retreating sides of the stir track also showed increases, albeit less than that seen in the stir zone, increasing by 37% and 33% respectively.

By considering the macrostructural differences of the stir track, the differences in the average hardness of the different regions of stir track can be explained. In the middle of the stir track lies the stir zone which showed the greatest increase in hardness. This region (Figure 31 (a)) was seen to contain material that had been severely strained and plastically deformed directly by the rotating pin and shoulder of the tool, affecting the surface and subsurface material. Meanwhile, the material on the advancing and retreating sides had been deformed by the shoulder of the tool, affecting only the surface material of the stir track. This would have equated to a reduced severity of deformation and depth of affected material, and accordingly, lesser hardness gains relative to the starting sintered material.

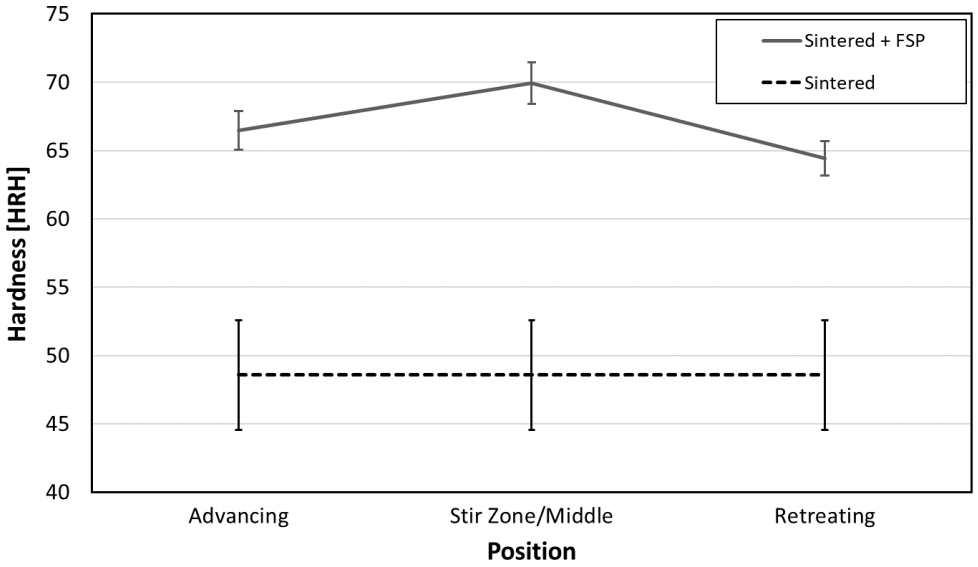

Figure 35 - Comparison of the average surface hardness values measured in different regions of TC2000 test specimens (Sintered vs. Sintered + FSP). FSP conditions of 90 mm min^{-1} @ 900 RPM were utilized.

Chapter 7.0 Conclusions

The research carried out in this study attempted to determine the response of two commercial APM alloys to FSP and FSW. The alloys investigated were PM2618 (Al-2.3Cu-1.6Mg-1Fe-1Ni-0.5Sn) and TC2000 (Al-1Mg-1.5Sn). The affects of varying tool rotation speeds and traverse rates were the primary focus of the investigation. It was found that while the PM2618 alloy responded highly favourably under several different processing parameter conditions, the TC2000 alloy responded very poorly and was unable to successfully be stir processed without defects occurring.

A combination of X-ray radiography and microstructural analyses (both SEM and optical) was used to confirm the presence/absence of defects in the alloys, and confirmed that PM2618 could be successfully processed via FSP and FSW under a variety of process parameter combinations, while TC2000 could not. FSP and FSW were found to result in significant microstructural refinement within the SZ. This was manifested as a reduced grain size, enhanced homogeneity in terms of secondary phase size/distribution, and the elimination of residual porosity. By using XRD it was found that the physical changes to the microstructure in both alloys had no discernable alterations to the nominal phase composition.

Hardness of the non-heat treated (T1) samples of both alloys increased as a result of FSP/FSW but the gains were found to vary through the stirred cross sections. A T6 heat treatment applied to the PM2618 (TC2000 is not heat treatable) improved the hardness further but resulted in the as-sintered and the FSP/FSW materials having comparable hardness. Three-point bend testing was conducted in both static loading and fatigue loading, where it was confirmed that T1 FSW products of PM2618 significantly exhibited improved static bend strength properties as well as bending fatigue behaviour relative to the as-sintered material.

7.1 Future Work

The research conducted in this investigation was by no means all-encompassing, and due primarily to time and equipment constraints there remains additional research to be conducted in this area including:

1. Expand the envelope of successful processing parameters for PM2618. While this research was limited to a maximum traverse rate of 180 mm/min, a higher speed may be more desirable from an industrial standpoint to expedite processing.
2. Investigate the mechanical loads and temperatures experienced during FSP/FSW using successful processing parameters.
3. Explore the mechanical properties of FSW PM2618 once T6 heat treated.
4. Employ EBSD to investigate microstructural and recrystallization behaviour differences between heat treatable and non-heat treatable APM alloys after FSP.
5. Broaden the parameter range investigated for TC2000 to ensure that appropriate FSW conditions were not inadvertently missed. This effort could also include investigating additional parameters such as tool design, material preheating, and tool tilt angle.
6. Investigate the applicability of the successful processing parameters from this research to other APM alloys of the 2xxx series.

References

[1] R. M. German, *Powder Metallurgy & Particulate Materials Processing*. Princeton, NJ: Metal Powder Industry, 2005.

[2] A. Upadhyaya and G. S. Upadhyaya, *Powder Metallurgy: Science, Technology, and Materials*. University Press, 2011.

[3] C. D. Boland, R. L. Hexemer, I. W. Donaldson, and D. P. Bishop, "On the Development of an Aluminum PM Alloy for 'Press-Sinter-Size' Technology," *Int. J. Powder Metall.*, vol. 47, no. 1, pp. 39–48, 2011.

[4] W. D. Judge, D. P. Bishop, and G. J. Kipouros, "Effect of sizing on the corrosion behaviour of Alumix 123 P/M alloy in 3.5 wt-% NaCl solution," *Corros. Eng. Sci. Technol.*, vol. 52, no. 1, pp. 29–37, 2017.

[5] W. D. Callister and D. G. Rethwisch, *Materials Science and Engineering An Introduction*, 9th ed. Hoboken, NJ: John Wiley & Sons Ltd., 2014.

[6] G. . Schaffer, T. . Sercombe, and R. . Lumley, "Liquid phase sintering of aluminium alloys," *Mater. Chem. Phys.*, vol. 67, no. 1, pp. 85–91, 2001.

[7] R. N. Lumley and G. B. Schaffer, "The effect of solubility and particle size on liquid phase sintering," *Scr. Mater.*, vol. 35, no. 5, pp. 589–595, 1996.

[8] G. S. Upadhyaya, *Sintered Metallic and Ceramic Materials - Preparation, Properties and Applications*. John Wiley & Sons Ltd., 2000.

[9] G. B. Schaffer, B. J. Hall, S. J. Bonner, S. H. Huo, and T. B. Sercombe, "The effect of the atmosphere and the role of pore filling on the sintering of aluminium," *Acta Mater.*, vol. 54, no. 1, pp. 131–138, 2006.

[10] ASM International, *ASM Handbook Volume 7: Powder Metal Technologies and Applications*, 2nd ed., vol. 7. Materials Park, OH, 1998.

[11] R. N. Lumley, T. B. Sercombe, and G. B. Schaffer, "Surface oxide and the role of magnesium during the sintering of aluminum," *Metall. Mater. Trans. A Phys. Metall. Mater. Sci.*, vol. 30, no. 2, pp. 457–463, 1999.

[12] A. Kimura *et al.*, "Reduction mechanism of surface oxide in aluminum alloy powders containing magnesium studied by x-ray photoelectron spectroscopy using synchrotron radiation," *Appl. Phys. Lett.*, vol. 70, no. 26, pp. 3615–3617, 1997.

[13] K. Kondoh, A. Kimura, and R. Watanabe, "Analysis of tin behaviour on surface of rapidly solidified aluminium alloy powder particles during heating," *Powder Metall.*, vol. 44, no. 3, pp. 253–258, 2003.

[14] D. Kent, G. B. Schaffer, M. Qian, and Z. Y. Liu, “Formation of Aluminium Nitride during Sintering of Powder Injection Moulded Aluminium,” *Mater. Sci. Forum*, vol. 618–619, pp. 631–634, 2009.

[15] S. P. Ringer, B. T. Sofyan, K. S. Prasad, and G. C. Quan, “Precipitation reactions in Al-4.0Cu-0.3Mg (wt.%) alloy,” *Acta Mater.*, vol. 56, no. 9, pp. 2147–2160, 2008.

[16] S. C. Wang and M. J. Starink, “Two types of S phase precipitates in Al-Cu-Mg alloys,” *Acta Mater.*, vol. 55, no. 3, pp. 933–941, 2007.

[17] R. W. Cooke, R. L. Hexemer, I. W. Donaldson, and D. P. Bishop, “Powder metallurgy processing of Al-Cu-Mg alloy with low Cu/Mg ratio,” *Powder Metall.*, vol. 55, no. 1, pp. 29–35, 2012.

[18] D. P. Bishop, B. Hofmann, and K. R. Couchman, “Properties and Attributes of Commercially Available AC2014-Type Aluminum P/M Alloys,” in *Advances in Powder Metallurgy and Particulate Materials*, H. Ferguson and D. T. Whychell, Eds. MPIF, 2000, pp. 87–100.

[19] D. P. Bishop, R. M. McNally, and T. Geiman, *Metallurgical Considerations in the Development and Manufacture of Aluminum P/M Camshaft Bearing Caps*. MPIF, 2000.

[20] C. D. Boland, R. L. Hexemer, I. W. Donaldson, and D. P. Bishop, “Industrial processing of a novel Al-Cu-Mg powder metallurgy alloy,” *Mater. Sci. Eng. A*, vol. 559, pp. 902–908, 2013.

[21] R. W. Cooke, R. L. Hexemer, I. W. Donaldson, and D. P. Bishop, “Press-and-sinter processing of a PM counterpart to wrought aluminum 2618,” *J. Mater. Process. Technol.*, vol. 230, pp. 72–79, 2016.

[22] L. J. B. Smith, R. L. Hexemer, I. W. Donaldson, and D. P. Bishop, “Development, Properties, and Applications for a High Thermal Conductivity Sintered Aluminum Material,” in *Proceedings of the 2012 International Conference on Powder Metallurgy and Particulate Materials*, 2012, pp. 170–180.

[23] L. J. B. Smith, S. F. Corbin, R. L. Hexemer, I. W. Donaldson, and D. P. Bishop, “Development and processing of novel aluminum powder metallurgy materials for heat sink applications,” *Metall. Mater. Trans. A Phys. Metall. Mater. Sci.*, vol. 45, no. 2, pp. 980–989, 2014.

[24] I. W. Donaldson, “High thermal conductivity aluminum powder metallurgy materials,” *Mater. Sci. Forum*, vol. 783–786, pp. 120–125, 2014.

[25] W. F. Smith, *Structure and Properties of Engineering Alloys*, 2nd ed. New York, NY: McGraw-Hill Inc., 1993.

[26] D. W. Heard, I. W. Donaldson, and D. P. Bishop, “Metallurgical assessment of a hypereutectic aluminum-silicon P/M alloy,” *J. Mater. Process. Technol.*, vol. 209, no. 18–19, pp. 5902–5911, 2009.

[27] A. D. P. LaDelpha, H. Neubing, and D. P. Bishop, “Metallurgical assessment of an emerging Al-Zn-Mg-Cu P/M alloy,” *Mater. Sci. Eng. A*, vol. 520, no. 1–2, pp. 105–113, 2009.

[28] American Welding Society, *Brazing Handbook*, Fifth. Miami, FL: American Welding Society, 2007.

[29] P. Roberts, *Industrial Brazing Practice*, 2nd ed. Boca Raton, FL: CRC Press, 2013.

[30] V. F. Khorunov and O. M. Sabadash, “9 - Brazing of aluminium and aluminium to steel,” in *Woodhead Publishing Series in Welding and Other Joining Technologies*, Woodhead Publishing Limited, 2013, pp. 249–279.

[31] Solvay Special Chemicals, *NOCOLOK ® Encyclopedia*, 2nd ed. Hannover, Germany: Ahlers Heinel Werbeagentur GmbH, 2013.

[32] D. Lauzon, “Product Inquiry.” 2017.

[33] H. Zhao, S. Elbel, and P. Hrnjak, “Controlled atmosphere brazing of aluminum heat exchangers,” *Weld. J. Brazing Solder. Today*, vol. 92, no. 2, pp. 44–46, 2013.

[34] B. M. Ponchei, “Removal of Flux From Brazed Aluminum Assemblies,” US 3196113 A, 1965.

[35] T. Murase and Y. Yanagawa, “Effects of flow of liquid filler metal and base metal composition on erosion characteristics during aluminium brazing,” *Weld. Int.*, vol. 24, no. 1, pp. 6–12, 2010.

[36] M. Qian and G. B. Schaffer, “12 - Sintering of aluminum and its alloys,” *Sinter. Adv. Mater. - Fundam. Process.*, no. 2, pp. 289–323, 2010.

[37] Australian Government Department of Environment and Energy, “Magnesium oxide fume: Sources of emissions.” .

[38] L. Orman, “Flux Residues of Aluminium Brazing and Engine Coolants.”

[39] Y. Hisatomi, “Recent advance of brazing sheet and flux for aluminium brazing,” *Weld. Int.*, vol. 22, no. 7, pp. 421–426, 2008.

[40] Solvay Special Chemicals, *The NOCOLOK ® Flux Brazing Process*. Hannover, Germany: Ahlers Heinel Werbeagentur GmbH.

[41] P. L. Threadgill, A. J. Leonard, H. R. Shercliff, and P. J. Withers, “Friction Stir Welding of Aluminium Alloys,” *Int. Mater. Rev.*, vol. 54, no. 2, pp. 49–93, 2009.

[42] G. Madhusudhan Reddy and A. A. Gokhale, “Welding aspects of aluminum-lithium alloys,” in *Aluminum-Lithium Alloys: Processing, Properties, and Applications*, Elsevier Inc., 2013, pp. 259–302.

[43] J. Ding, B. Carter, K. Lawless, A. Nunes, M. Suites, and J. Schneider, “A Decade of Friction Stir Welding R&D At NASA’s Marshall Space Flight Center And a Glance into the Future,” Huntsville, AL, United States, 2006.

[44] Lockheed Martin Space Systems, “Fact Sheet Space Shuttle External Tank,” New Orleans, LA, 2008.

[45] S. W. Kallee, *Industrial applications of friction stir welding*. Woodhead Publishing Limited, 2009.

[46] D. Lohwasser and Z. Chen, “Introduction,” in *Friction Stir Welding: From Basics to Applications*, 2009, pp. 1–12.

[47] S. W. Kallee and J. Davenport, “Trends in design and fabrication of rolling stock,” *European Railway Review*, vol. 13, no. 1, 2007.

[48] A. Amini, P. Asadi, and P. Zolghadr, *Friction stir welding applications in industry*. Woodhead Publishing Limited, 2014.

[49] S. W. Kallee, J. M. Kell, W. M. Thomas, and C. S. Wiesner, “Development and implementation of innovative joining processes in the automotive industry,” in *Paper presented at DVS Annual Welding Conference “Große Schweißtechnische Tagung”, Essen, Germany, 12-14 September 2005*, 2005.

[50] ASM International, *ASM Handbook Volume 8: Mechanical Testing and Evaluation*. Materials Park, OH: ASM International, 2000.

[51] American Welding Society, “AWS D17.3/D17.3M:2016 - Specification for Friction Stir Welding of Aluminum Alloys for Aerospace Applications.” American Welding Society, p. 58, 2016.

[52] International Organization for Standardization, “BS EN ISO 5173:2010+A1:2011 - Destructive tests on welds in metallic materials - Bend tests.” International Organization for Standardization, Geneva, Switzerland, 2010.

[53] ASM International, “Fatigue Testing,” in *Atlas of Fatigue Curves*, 1st ed., H. E. Boyer, Ed. Materials Park, Ohio: ASM International, 1986, p. 510.

[54] International Organization for Standardization, “ISO/TR 14345:2012 - Fatigue testing of welded components - Guidance.” International Organization for Standardization, Geneva, Switzerland, p. 32, 2012.

[55] R. Nandan, T. DebRoy, and H. K. D. H. Bhadeshia, “Recent advances in friction-stir welding - Process, weldment structure and properties,” *Prog. Mater. Sci.*, vol. 53, no. 6, pp. 980–1023, 2008.

[56] ASM International, *ASM Metals Handbook - Vol. 6: Welding, Brazing, and Soldering*, 10th ed., vol. 6. Materials Park, Ohio: ASM International, 1993.

[57] ASM International, *ASM Metals Handbook - Vol. 2: Properties and Selection: Nonferrous Alloys and Special-Purpose Materials*, 10th ed., vol. 2. Materials Park, Ohio: ASM International, 1990.

[58] S. Benavides, Y. Li, L. E. Murr, D. Brown, and J. C. McClure, "Low-temperature friction-stir welding of 2024 aluminum," *Scr. Mater.*, vol. 41, no. 8, pp. 809–815, 1999.

[59] M. J. Jones, P. Heurtier, C. Desrayaud, F. Montheillet, D. Allehaux, and J. H. Driver, "Correlation between microstructure and microhardness in a friction stir welded 2024 aluminium alloy," *Scr. Mater.*, vol. 52, no. 8, pp. 693–697, 2005.

[60] W. F. Xu, J. H. Liu, D. L. Chen, and G. H. Luan, "Low-cycle fatigue of a friction stir welded 2219-T62 aluminum alloy at different welding parameters and cooling conditions," *Int. J. Adv. Manuf. Technol.*, vol. 74, no. 1–4, pp. 209–218, 2014.

[61] S. Di, X. Yang, G. Luan, and B. Jian, "Comparative study on fatigue properties between AA2024-T4 friction stir welds and base materials," *Mater. Sci. Eng. A*, vol. 435–436, pp. 389–395, 2006.

[62] T. Le Jolu, T. F. Morgeneyer, A. Denquin, and A. F. Gourgues-Lorenzon, "Fatigue lifetime and tearing resistance of AA2198 Al-Cu-Li alloy friction stir welds: Effect of defects," *Int. J. Fatigue*, vol. 70, pp. 463–472, 2015.

[63] ASTM International, "B595-11(2016) Standard Specification for Sintered Aluminum Structural Parts." ASTM International, West Conshohocken, PA, 2016.

[64] G. A. Sweet, R. L. Hexemer, I. W. Donaldson, A. Taylor, and D. P. Bishop, "Powder metallurgical processing of a 2xxx series aluminum powder metallurgy metal alloy reinforced with AlN particulate additions," *Mater. Sci. Eng. A*, vol. 755, no. April, pp. 10–17, 2019.

[65] MPIF, "2018 Award-Winning Powder Metal Parts," 2018. [Online]. Available: https://www.mpif.org/News/TabId/164/ArtMID/586/ArticleID/106/2018-Award-Winning-Powder-Metal-Parts.aspx. [Accessed: 29-Aug-2019].

[66] Metal Powder Industries Federation, *Standard Test Methods for Metal Powders and Powder Metallurgy Products*. Princeton, NJ: MPIF, 2012.

[67] N. R. Reddy and G. M. Reddy, "Friction stir welding of aluminium alloys," *Int. J. Mech. Eng. Technol.*, vol. 7, no. 2, pp. 83–90, 2016.

[68] P. Kah, R. Rajan, J. Martikainen, and R. Suoranta, "Investigation of weld defects in friction-stir welding and fusion welding of aluminium alloys," *Int. J. Mech. Mater. Eng.*, vol. 10, no. 1, 2015.

[69] G. A. W. Sweet *et al.*, “Microstructural evolution of a forged 2XXX series aluminum powder metallurgy alloy,” *Mater. Charact.*, vol. 151, no. January, pp. 342–350, 2019.

[70] L. Wang, C. M. Davies, R. C. Wimpory, L. Y. Xie, and K. M. Nikbin, “Measurement and simulation of temperature and residual stress distributions from friction stir welding AA2024 Al alloy,” *Mater. High Temp.*, vol. 27, no. 3, pp. 167–178, 2010.

[71] W. Tang, X. Guo, J. C. McClure, L. E. Murr, and A. Nunes, “Heat input and temperature distribution in friction stir welding,” *J. Mater. Process. Manuf. Sci.*, vol. 7, no. 2, pp. 163–172, 1998.

[72] B. Li, Y. Shen, and W. Hu, “The study on defects in aluminum 2219-T6 thick butt friction stir welds with the application of multiple non-destructive testing methods,” *Mater. Des.*, vol. 32, no. 4, pp. 2073–2084, 2011.

[73] H. J. Liu, Y. C. Chen, and J. C. Feng, “Effect of zigzag line on the mechanical properties of friction stir welded joints of an Al-Cu alloy,” *Scr. Mater.*, vol. 55, no. 3, pp. 231–234, 2006.

[74] M. Wilson *et al.*, “Hot extrusion of a commercial aluminum powder metallurgy metal matrix composite material,” *J. Mater. Perform. Charact.*, vol. In Press, 2019.

[75] P. Ghosh, M. Mezbahul-Islam, and M. Medraj, “Critical assessment and thermodynamic modeling of Mg-Zn, Mg-Sn, Sn-Zn and Mg-Sn-Zn systems,” *Calphad Comput. Coupling Phase Diagrams Thermochem.*, vol. 36, pp. 28–43, 2012.

Appendix A - Tensile Specimen Geometries for FSW Joints

Standard AWS D17.3/D17.3M:2016

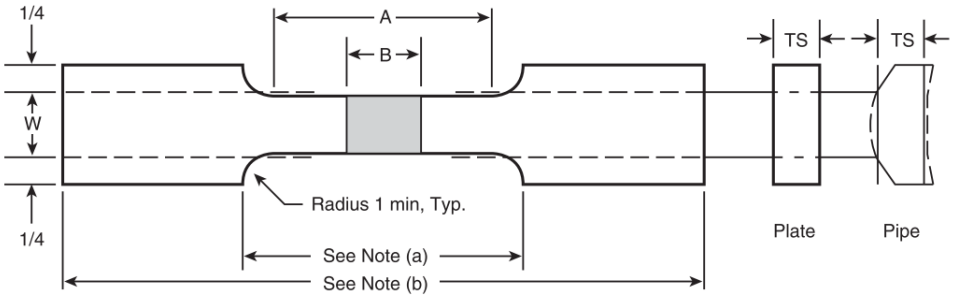

in	mm
1/4	6.4
1/2	13
3/4	19
1	25
3	76

Test Weldment			
		Pipe	
		Outside Diameter	
Dimensions	Plate	<3	>3
B	← See Note (c) →		
A	← See Note (d) →		
W	3/4	1/2	3/4
TS	TS[e]	← See Note (e) →	

All Dimensions in Inches

Notes:

[a] This section shall be cut by machining or grinding.

[b] The specimen length shall be as required by the tension testing equipment.

[c] Dimension B shall be equal to the greater dimension of the weld metal in the direction of the specimen's longitudinal axis.

[d] The length of the reduced section A shall be equal to B plus 1/2 in [13 mm] with a minimum of 2-1/4 in [57 mm]. The ends shall not differ in width from the ends to the center, but the width at either end shall not be more than 0.015 in [0.38 mm] greater than the width at the center. The weld shall be in the center of the reduced section.

[e] The amount removed shall be the minimum needed to obtain plane parallel surfaces across the width of the reduced section.

Source: Adapted from AWS B2.1:2000, *Specification for Welding Procedure and Performance Qualification*, Figure II-3A.

Figure 36 - Rectangular Section Tensile Specimen.

in	mm
.188	4.77
.250	6.35
.350	8.89
.500	12.70
1/4	6.4
3/8	9.5
1/2	13
3/4	19

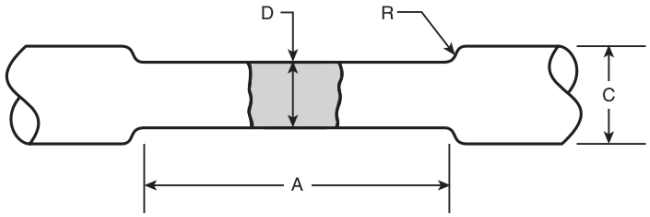

	Standard Specimen Dimension, in.[a,b]			
Dimensions	0.505	0.353	0.252	0.188
A = Length of Reduced Section[c,d]	← See Note (d) →			
D = Diameter	0.500 ± 0.010	0.350 ± 0.007	0.250 ± 0.005	0.188 ± 0.003
R = Radius, Inches minimum	3/8 min.	1/4 min.	3/16 min.	1/8 min.
C = Diameter	3/4	1/2	3/8	1/4

Notes:

[a] The standard specimen that is selected shall be based upon the maximum diameter specimen that can be cut from the specimen blank.

[b] Where only a single specimen from a blank is required, the specimen's longitudinal axis shall be centered between the base metal surfaces.

[c] The weld shall be in the center of the reduced section.

[d] The length of the reduced section shall be not less than the width of the weld metal plus 2D. It may have a gradual taper from the ends toward the center, with the ends not more than one percent greater in diameter than the center, which shall be the dimension D. The ends may be of any length and shape as required by the testing machine.

Figure 37 - Round Section Tensile Specimen